

Time-Dependent Decrease in Fault Strength in the 2011–2016 North Kanto Earthquake Sequence

Sam Wimpenny^{1,2*}, Natalie Forrest^{1,2+} and Alex Copley¹

¹COMET, Bullard Laboratories, Department of Earth Sciences,
University of Cambridge, UK

²COMET, Department of Earth and Environment, University of Leeds, UK

Emails: **earswi@leeds.ac.uk* and +*eenlef@leeds.ac.uk*

1 Key Points:

- 2 • We model the evolution of stress and slip on the Mochiyama Fault between two near-identical
3 M_w 5.8 earthquakes.
- 4 • Models that match the observed surface deformation can only reload the Mochiyama Fault by
5 35–50% of the first earthquake's coseismic stress drop.
- 6 • At least a 2–10 MPa decrease in the shear stresses needed to break the Mochiyama Fault in
7 earthquakes is needed to explain the short inter-event time.

8

9 *This paper is a pre-print, therefore has not been through peer review and is currently being considered*
10 *for publication in Geophysical Journal International.*

Abstract

Two near-identical M_w 5.8 earthquakes in 2011 and 2016 ruptured the Mochiyama Fault in North Kanto, Japan. The unusually short repeat time between the Mochiyama earthquakes provides a rare opportunity estimate the evolution of stress on a fault through an earthquake cycle, as the stress drop in the first earthquake provides a reference from which we can infer variations through time in the stresses required to cause earthquake rupture. By combining observations of deformation from GPS, InSAR and seismology with numerical models of stress transfer due to coseismic deformation and postseismic relaxation, we demonstrate that the rupture area on the Mochiyama Fault could only have been re-loaded by 35–50% of the 2011 earthquake stress drop over the period between the 2011 and 2016 earthquakes. We infer that the Mochiyama Fault became weaker in the intervening 6 years, with a 2–10 MPa drop in the shear stresses needed to break the fault in earthquakes. The mechanism(s) that led to this weakening are unclear, but were associated with extensive aftershock seismicity that released a cumulative moment similar to the 2011 mainshock. Temporal changes in fault strength may therefore play a role in modulating the timing of moderate-magnitude earthquakes.

25 1 Introduction

26 Earthquakes are generated by the accumulation of elastic strain around a fault zone, and its eventual
27 release when the shear stress resolved on the fault exceeds the frictional resistance to slip [Reid,
28 1910]. However, a deterministic application of this ‘elastic rebound theory’ to estimate the timing of
29 large earthquakes has proven difficult [e.g. Roeloffs and Langbein, 1994], because the absolute state
30 of stress on faults cannot be easily measured, the evolution of stress and strain between earthquakes
31 is typically too long to be inferred from geodetic measurements of deformation, and the strength of
32 active faults, and how fault strength varies in space, remains a controversial topic. In addition, where
33 the timing of multiple earthquakes on a particular fault patch are well documented, they sometimes
34 show non-periodic repeat times [Murray and Segall, 2002; Sieh et al., 2008; Fukushima et al., 2018].
35 This observation suggests that, at least in some cases, the rate of fault loading, or fault strength, may
36 also vary with time to produce ‘non-characteristic’ earthquakes on faults [Kagan et al., 2012].

37 Two near-identical M_w 5.8 normal-faulting earthquakes near Mochiyama in North Kanto, Japan on
38 the 19th March 2011 and 28th December 2016 provide a rare opportunity to determine the evolution of
39 stress on a fault through a whole earthquake cycle (Figure 1). A previous study of the slip distributions
40 in the Mochiyama earthquakes demonstrated that the two events ruptured the same area of the NNW-
41 SSE striking Mochiyama Fault between the surface and 7 km depth (Figure 1b,c) [Fukushima et al.,
42 2018]. Therefore the same patch of fault reached its failure stress twice in the space of ~ 6 years.
43 Between the two earthquakes, Japan’s GPS network captured significant extensional strain across the
44 Mochiyama Fault. Fukushima et al. [2018] argued that this deformation may reflect rapid reloading
45 of the fault through extensive postseismic afterslip, though also found that a model of afterslip driven
46 by coseismic stress changes could only account for a small fraction of the observed inter-event strain,
47 and could only reload the Mochiyama Fault by $<10\text{--}20\%$ of the coseismic stress drop.

48 The Mochiyama earthquakes formed part of a sequence of seismicity in North Kanto that began
49 after the 11th March 2011 M_w 9.1 Tohoku-oki earthquake, and which included three other moderate-
50 magnitude earthquakes within 20 km of Mochiyama in March and April 2011 [Imanishi et al., 2012;
51 Fukushima et al., 2013] (Figure 1a). These earthquakes generated coseismic displacements in North
52 Kanto that will have changed the stress state on the Mochiyama Fault [King et al., 1994]. The coseismic
53 stress changes will have been at least partially relaxed through afterslip and aftershocks within the
54 seismogenic crust, and distributed viscous flow or localised viscous shear within the aseismic lower
55 crust and upper mantle [Freed, 2005], causing time-dependent stress changes on the Mochiyama Fault

56 between 2011 and 2016. As all of these stress changes were not included in the original calculations of
57 Fukushima et al. [2018], and because their calculations could not account for the observed deformation,
58 it remains unclear whether the Mochiyama Fault was fully reloaded back to its former failure stress,
59 or whether the fault became weaker and ruptured at a lower failure stress in 2016. Addressing this
60 question is clearly critical to developing our understanding of the controls on the strength of active
61 faults and for building deterministic models of the earthquake cycle and seismic hazard.

62 In this study, we build upon the work of Fukushima et al. [2018] and determine the coseismic and time-
63 dependent stress changes on the Mochiyama Fault throughout the North Kanto earthquake sequence.
64 We then use these stress change calculations to investigate potential temporal changes in the fault-
65 averaged failure strength. We begin by making new geodetic and seismological observations of the
66 earthquake sequence in Section 2 to place constraints on the mechanisms that loaded the Mochiyama
67 Fault. We then develop a series of forward models in Section 3 to determine by how much each different
68 mechanism could have reloaded the Mochiyama Fault within the limits of the observed deformation.
69 These models extend the previous work of Fukushima et al. [2018] by: (1) gaining more general insight
70 into the ways postseismic relaxation reloads fault zones, and (2) by performing a much wider range
71 of models that allow us to assess how variations in the rheology of the Earth might translate into
72 estimates of fault reloading and surface strain. From our modelling we find that the Mochiyama
73 Fault could only have been reloaded by less than half of the average coseismic stress drop of the
74 2011 earthquake by the time the 2016 earthquake re-ruptured the fault. In Section 4, we discuss the
75 implications of this result for the time-dependent strength of active faults.

76 **2 Observations of the North Kanto Earthquake Sequence**

77 **2.1 Long-Period Body-Waveform Modelling**

78 We first determined the focal mechanisms, centroid depths, source-time functions and moment releases
79 of the 2011 and 2016 Mochiyama earthquakes by inverting their long-period teleseismic P and SH
80 seismograms using synthetic waveforms of the P , S , pP , sP and sS phases, modelled assuming a
81 finite-duration rupture at a point source [Nabalek, 1984; Zwick et al., 1994]. This method has been
82 widely used and described, because of its sensitivity to the mechanisms and centroid depths of shallow
83 moderate-magnitude earthquakes [e.g. McCaffrey and Abers, 1988; Taymaz et al., 1990]. Therefore
84 further details of the modelling are provided in Supplementary Text S1.

85 The long-period waveforms of both earthquakes can be well matched at most stations using this
86 method (Figure 2). The minimum-misfit solution for the 2011 earthquake has a seismic moment of
87 4.7×10^{17} Nm (M_w 5.7), a source-time function length of 3 seconds, a strike/dip/rake of the south-
88 west dipping nodal plane of 144/43/292 and a 5 km centroid depth (Figure 2a). The moment is
89 similar to estimates from the USGS W-Phase (4.3×10^{17} Nm), USGS body-wave (4.5×10^{17} Nm) and
90 Global Centroid Moment Tensor (6.9×10^{17} Nm) methods, but is only 40% of that derived from the
91 InSAR-based coseismic slip inversion of Fukushima et al. [2018] when calculated using the same shear
92 modulus (1.2×10^{18} Nm). The 2016 earthquake has a near-identical minimum-misfit solution to the
93 2011 earthquake, with a moment release of 5.4×10^{17} Nm, a source-time function length of 4 seconds,
94 a strike/dip/rake of 131/40/282 and a centroid depth of 4 km (Figure 2b). The seismic moment
95 estimate is identical to the geodetic moment derived by Fukushima et al. [2018] when using the same
96 shear modulus (5.4×10^{17} Nm). For both earthquakes, the centroid depth and moment release trade-off
97 against one another, as at shallower depths the depth-phases destructively interfere with the direct
98 phase meaning a larger moment is needed to account for waveforms of a given amplitude [Taymaz
99 et al., 1990]. By varying the centroid depth during the inversions between 3 km and 7 km, which is
100 the InSAR-derived range of peak coseismic slip [Fukushima et al., 2018], the minimum-misfit moment
101 release in both earthquakes ranges from $3\text{--}6 \times 10^{17}$ Nm.

102 Given that the amplitude of postseismic deformation scales with the coseismic moment [Churchill
103 et al., 2022], our new estimate of the coseismic moment of the 2011 Mochiyama earthquake will
104 have important implications for the predicted postseismic deformation. The likely explanation for
105 the difference between the seismic and geodetic moment estimates is that the interferograms used to
106 invert for the pattern of coseismic slip contained some surface deformation from a series of shallow
107 M_w 4–5 earthquakes that pre-date the 19th March event. These earthquakes were located within the
108 hangingwall of the Mochiyama Fault, and align along a north-east dipping conjugate plane seen in the
109 relocated aftershock seismicity (Supplementary Figure 1). By mapping the surface deformation from
110 these small, shallow earthquakes into deep coseismic slip on the Mochiyama Fault, we suggest that
111 Fukushima et al. [2018] overestimated the moment release in the 2011 earthquake. In the following
112 sections, we show that the GPS and microseismicity measurements support this conclusion.

113 2.2 GPS

114 We collected the daily position time-series from each GPS station in Japan’s GEONET network and
115 used a trajectory-modelling approach with a common-mode filter to calculate the displacement field in

116 North Kanto [e.g. Bedford et al., 2020]. The vertical and horizontal displacements were dominated by
117 an eastward translation and uplift caused by postseismic relaxation after the Tohoku-oki earthquake.
118 Therefore, to study the evolution of deformation in our study region, we calculated the 2-D incremental
119 strain tensor over different epochs using the triangular interpolation method of Bourne et al. [1998].
120 This method does not enforce any smoothing on the strain field, therefore can identify strain signals
121 on the length scale of the station spacing. Residuals between the trajectory models and the GPS
122 time-series, which we interpret to represent random noise that is not caused by deformation, were
123 consistently Gaussian with a standard deviation of 2–3 mm. This noise translates into an uncertainty
124 of ~ 0.2 – 0.3 microstrain given the typical station spacing in the network of 15–20 km. The vertical
125 displacements do not contain any clear signals related to the Mochiyama earthquake sequence beyond
126 those associated with the coseismic displacements, and therefore we do not consider them further here.

127 The 2-D incremental strain field through time is shown in Figure 3. The first epoch covers the 19th
128 March 2011 earthquake on the Mochiyama Fault, which generated predominantly 1.6 microstrain
129 of ENE-WSW extension in the 10–15 km-wide triangles spanning the fault zone, and predominantly
130 contraction in triangles to the south-west of the fault (Figure 3a). In the month that followed, the GPS
131 network recorded a further 1.2 microstrain of NE-SW extension across the Mochiyama Fault (Figure
132 3b), and 4–5 microstrain of NW-SE extension generated by a M_w 5.9 normal-faulting earthquake on
133 the 23rd March 2011 [Fukushima et al., 2013] (Figure 3b). Outside of the epicentral region of these
134 earthquakes, North Kanto was being stretched \sim E–W by 0.2–0.4 microstrain as a result of ongoing
135 postseismic relaxation following the Tohoku-oki earthquake [Ozawa et al., 2011; Hu et al., 2016].

136 The largest earthquake within the sequence occurred on the 11th April 2011: a M_w 6.6 earthquake
137 that simultaneously ruptured two NW-SE trending normal faults 20 km north of Mochiyama near the
138 city of Iwaki (known herein as the ‘Iwaki Faults’). The Iwaki earthquake was followed a day later by a
139 M_w 5.9 strike-slip aftershock. These two earthquakes generated 20–25 microstrain of extension across
140 the Iwaki Faults and 0.7 microstrain of extension across the Mochiyama Fault (Figure 3c).

141 Between May 2011 and December 2016 there were no more $M_w > 5$ earthquakes in North Kanto. GPS
142 stations that span the Mochiyama Fault measured 2–3 microstrain of ENE-WSW extension (Figure
143 3d) that followed a logarithmic decay in time. Elsewhere, almost all of North Kanto experienced ~ 2
144 microstrain of shear with the maximum principal strain axis being oriented \sim E–W to NW-SE, and
145 the minimum principal strain axis oriented \sim N–S to NE-SW. This regional pattern of shear strain
146 represents the deformation of the Japanese mainland caused by postseismic relaxation following the
147 Tohoku-oki earthquake [e.g. Hu et al., 2016; Becker et al., 2018].

148 The cumulative strain between the 2011 and 2016 Mochiyama earthquakes (the ‘inter-event period’)
149 represents the deformation that could have reloaded the Mochiyama Fault (Figure 3e). The strain
150 across the fault was consisted of 3.8–4.3 microstrain of extension — 0.7 microstrain of which can be
151 attributed to the static deformation caused by the Iwaki earthquakes. Any model of the reloading
152 of the Mochiyama Fault must account for the remaining 3.1–3.6 microstrain of across-fault stretching
153 through predominantly aseismic deformation mechanisms. Within the triangles to the south-west
154 of the fault that span the fault’s hangingwall, the strain field consisted of incremental contraction.
155 Notably, the principal strain axes in triangles that span the Mochiyama Fault, and triangles in the
156 immediate fault hangingwall, are sub-parallel to the principle axes of the coseismic strain field in the
157 2011 Mochiyama earthquake (compare Figure 3a with 3e). Therefore, the sense of aseismic strain
158 around the Mochiyama Fault over the inter-event period can be accounted for by postseismic aseismic
159 slip (‘afterslip’) on the mainshock fault plane within a similar depth-range to coseismic slip.

160 On the 28th December 2016 the second earthquake re-ruptured the Mochiyama Fault and gener-
161 ated 2 microstrain of ENE-WSW extension across the fault zone with a similar pattern to the 2011
162 earthquake (Figure 3f). The across-fault extension in 2016 was slightly larger than in 2011, which
163 supports the conclusion from the long-period body-waveform modelling that the 2016 earthquake had
164 a slightly larger moment release than in 2011. Over the postseismic period between December 2016
165 and December 2017, the GPS network captured ~ 0.3 microstrain of logarithmically-decaying post-
166 seismic extension across the Mochiyama Fault (Supplementary Figure 2), which was 10-times smaller
167 than the strain recorded in the year after the 2011 earthquake. Despite the stark difference in the
168 amplitude of the postseismic strain measured after the 2011 and 2016 Mochiyama earthquakes, the
169 relaxation time of the strain transients were near-identical (Supplementary Figure 3).

170 2.3 Radar Geodesy

171 Fukushima et al. [2018] and Komura et al. [2019] previously formed ALOS interferograms of the co-
172 seismic deformation in the 2011 and 2016 Mochiyama earthquakes (Figure 4a,c). The two earthquakes
173 generated near-identical patterns of coseismic surface deformation, suggesting the slip distributions
174 overlapped significantly at depth. The interferograms record peak line-of-sight (LOS) displacements
175 of 40–60 cm and a sharp offset in LOS across the north-western fault tip. The LOS displacements
176 decrease in amplitude, and become smoother, towards the south-eastern fault tip. These features of
177 the data suggest that peak slip in both earthquakes overlapped on the north-western portion of the
178 fault, and that slip became buried and decreased towards the south-east [Fukushima et al., 2018] (see

179 Figure 1b). Given that both earthquakes had similar seismic moment releases, and similar rupture
180 areas, then it is likely that they had similar stress drops.

181 For the 2011 Mochiyama earthquake, the coseismic interferogram shows an increase in the wavelength
182 of the hangingwall subsidence towards the southern edge of the fault (Figure 4a). This signal may
183 be related to more slip at depth along the southern portion of the Mochiyama Fault compared to
184 the north (as seen in Figure 1b), or could reflect the deformation caused by shallow M_w 4 and 5
185 normal-faulting earthquakes between the 11th March and 19th March 2011 (Figure 4a). Given that
186 the InSAR-derived slip model significantly overestimates the coseismic moment released determined
187 from long-period seismology in Section 2.1, we favour the latter interpretation.

188 To measure the postseismic deformation around the Mochiyama Fault, we formed Envisat ASAR
189 interferograms from the descending track 347 covering the first 7 months after the 2011 Mochiyama
190 earthquake. Envisat failed at the end of 2011, therefore we could only measure the early postseismic
191 deformation. The SAR data was processed using ISCE and a 30 m SRTM Digital Elevation Model [Farr
192 et al., 2007] to remove the topographic contribution to phase. The interferograms were unwrapped
193 using the statistical-cost network flow algorithm SNAPHU [Zebker and Lu, 1998]. We also applied a
194 Gaussian filter to the interferograms with a half-width of 0.5 km and removed a planar ramp.

195 Much of the region around the Mochiyama Fault is covered in thick vegetation, and therefore the
196 C-band data suffered from decorrelation. Nevertheless, in the month following the 2011 Mochiyama
197 earthquake one postseismic interferogram with good coherence could be formed (Figure 4b). A step
198 of $\sim 4\text{--}5$ cm in LOS displacement can be seen across the surface trace of the Mochiyama Fault. The
199 sharp offset in LOS displacement is mainly concentrated to the south-east of the area of peak coseismic
200 LOS displacement, which is a common observation following normal-faulting earthquakes and reflects
201 afterslip on the shallow portion of the mainshock rupture plane [e.g. Cheloni et al., 2010]. At distances
202 of $\sim 5\text{--}10$ km from the fault, the relative LOS displacements across the fault are $<1\text{--}2$ cm, which limits
203 the amount of deep afterslip or viscous flow that occurred in the first month after the 2011 earthquake.

204 We also formed interferograms using Sentinel-1 SAR data covering the first month of postseismic
205 deformation following the 2016 Mochiyama earthquake, using the same processing work flow. The
206 Sentinel-1 measurements reveal a sharp ~ 2 cm step in LOS displacement across the fault, and <1
207 cm of relative LOS displacement at distances >5 km from the surface trace of the fault (Figure 4d).
208 The patterns of near-field postseismic deformation are similar in the first month following the two
209 earthquakes. However, the 2016 earthquake was followed by less shallow afterslip.

2.4 Aftershock Seismicity

The locations, magnitudes and focal mechanisms of small earthquakes provide additional constraints on the deformation in the region of the Mochiyama Fault. We use the hypocentral locations determined by Uchide and Imanishi [2018], which are based on the Japan Meteorological Agency (JMA) unified catalogue that have been relatively re-located using the double-difference method [Waldhauser and Ellsworth, 2000]. Focal mechanisms derived by the National Research Institute for Earth Science and Disaster Resilience (NIED) provide additional constraints on the sources of microseismicity.

The 2011 Mochiyama earthquake was followed by a large number of normal-faulting aftershocks (Figure 5a) concentrated almost entirely between 5 km and 10 km depth (Supplementary Figure 4). The aftershocks were clustered around the margins and base of the rupture area, and delineate a planar structure dipping 40–60° towards the south-west [Kato et al., 2011]. Aftershocks recorded in the 2 years following the 2016 Mochiyama earthquake also had mostly normal-faulting mechanisms (Figure 5b), and were concentrated beneath the down-dip edge of the rupture area (Supplementary Figure 4). The similarity between the aftershock and the mainshock mechanisms, and the alignment of the microseismicity with the along-strike and down-dip projection of the mainshocks, imply that the aftershocks reflect slip on the Mochiyama Fault around the margins of the coseismic rupture.

Although the mechanisms and magnitudes of the 2011 and 2016 Mochiyama earthquakes were similar, the moment release in their aftershock sequences was significantly different (Figure 5c-f). The first six months after the 2011 earthquake was characterised by aftershock moment release that followed a logarithmic decay, mirroring the across-fault strain measured by the GPS network (Figure 5c,e). Most unusually, though, was that the cumulative moment release from aftershocks in the region directly around the Mochiyama Fault in the period May 2011 to December 2016 was $6 \pm 1 \times 10^{17}$ Nm, which is similar in magnitude to the 2011 mainshock moment release ($3\text{--}6 \times 10^{17}$ Nm). Aftershock sequences typically only account for between 1% and 20% of the mainshock moment [Zakharova et al., 2013], suggesting the seismicity that followed the 2011 Mochiyama earthquake was unusually energetic. The 2016 earthquake was followed by little across-fault extensional strain (Figure 5d) and a less energetic aftershock sequence that released only $1.8 \pm 0.3 \times 10^{17}$ Nm within 2 years of the mainshock (Figure 5f), which equates to a third of the mainshock moment release.

2.5 Summary of the Key Observations

The InSAR and body-waveform modelling show that the 2011 and 2016 earthquakes ruptured the same area of the Mochiyama Fault in two earthquakes with near-identical magnitudes. Over the inter-event period between these two earthquakes, the GPS network captured 3.1–3.6 microstrain of across-fault extension that could not be attributed to any moderate-magnitude seismicity. In GPS triangles that span the fault hangingwall, the sense of strain over the inter-event period was contractional. Postseismic InSAR observations demonstrated that some of this strain derived from at least 4–5 cm of shallow afterslip above the coseismic rupture on the Mochiyama Fault. Extensive aftershocks around the margins of the coseismic rupture suggest that afterslip was also prevalent at depth, extending down to at least 10 km. Summing the aftershock moment release over the aftershock cloud implies there was at least 20 cm of slip beneath the coseismic rupture over the inter-event period. Beneath 10 km there were few aftershocks, indicating that deformation was accommodated by predominantly aseismic deformation mechanisms. In the next section, we develop models of slip and stress on the Mochiyama Fault between the 2011 and 2016 earthquakes that attempt to match these constraints.

3 Modelling Stress Changes on the Mochiyama Fault

The observations point to three major sources of deformation in North Kanto between the Mochiyama earthquakes: (1) postseismic relaxation on and around the Mochiyama Fault, (2) coseismic deformation and postseismic relaxation from the nearby Iwaki earthquakes, and (3) regional postseismic relaxation following the Tohoku-oki earthquake. We take a forward-modelling approach to calculate how each source of deformation could have contributed to the pattern of surface strain, and the stress changes on the Mochiyama Fault, following the 2011 Mochiyama earthquake.

The time-series of deformation from the GPS and aftershock moment release indicate that the majority of the postseismic transient had finished by the time of the 2016 Mochiyama earthquake, suggesting that most of the coseismic stress changes imposed on the crust and mantle surrounding the fault had been relaxed, or balanced by elastic resistance to deformation in the seismogenic layer. We therefore keep the models as general as possible by calculating this ‘fully-relaxed’ state, and by fitting the pattern and amplitude of strain across the Mochiyama Fault, but not the temporal evolution of the strain. Considering only the fully-relaxed model has the benefit of making the estimates of reloading insensitive to the form of the constitutive laws that govern postseismic relaxation. We also make the

267 simplification that the background loading rate of the fault (the ‘interseismic deformation’) is small
 268 over the short time-frame between the two earthquakes, which is consistent with the lack of moderate-
 269 magnitude seismicity in the 50 years prior to the Mochiyama earthquakes in the gCMT catalogue
 270 [Ekström et al., 2012] and the paleoseismic record [Komura et al., 2019]. With these simplifications,
 271 it is the geometries of the imposed stresses and rheological components of the model domain, and the
 272 styles of postseismic relaxation, that control the magnitude of the fault reloading.

273 3.1 Generalised Models of Postseismic Reloading

274 To first gain an understanding of how local postseismic relaxation may have reloaded the Mochiyama
 275 Fault, we built a set of generalised stress-driven models that link coseismic slip to the postseismic
 276 reloading of the rupture area [e.g. Ellis and Stöckhert, 2004; Bagge and Hampel, 2017]. The models
 277 were designed to capture the maximum contribution of the three main postseismic deformation mech-
 278 anisms — afterslip, localised viscous shear and distributed visco-elastic relaxation — to reloading a
 279 normal fault after an earthquake [e.g. Freed and Lin, 1998]. The models also allow us to explore how
 280 uncertainties in our knowledge of the rheology of the crust and upper mantle in North Kanto will
 281 translate into uncertainties in the estimate of reloading of the Mochiyama Fault.

282 The model setup consists of a planar dip-slip fault of along-strike length L in a linear elastic layer
 283 of thickness z_e , which overlies a visco-elastic half-space (Figure 6). The elastic layer represents the
 284 seismogenic layer in the Earth in which elastic strain can accumulate and remain stored over the
 285 duration of an earthquake cycle. The visco-elastic half-space represents the depth below which the
 286 crust and mantle is hot enough that viscous creep can relax elastic stresses over an earthquake cycle.
 287 Spatially-uniform coseismic slip on the fault extends from the surface down to a depth z_r , and generates
 288 static stress changes in the surrounding medium. These static stress changes are then relaxed by
 289 viscous flow at depths $z > z_e$ and by afterslip at depths $0 \leq z \leq z_e$. In the fully-relaxed state, the
 290 afterslip zone down-dip of the coseismic rupture also approximates the behaviour of a thin (<200
 291 m-wide given the model discretisation) viscous shear zone surrounded by elastic wall rocks, therefore
 292 represents the case where deformation in the lower crust is accommodated in shear zones and not
 293 by distributed flow. The coseismic rupture remains locked and cannot slip post-seismically, therefore
 294 accumulates elastic strain and is reloaded as the surrounding regions deform.

295 The condition for frictional failure on a fault is described by the Coulomb criterion: $\tau - \mu'\sigma = 0$,
 296 where μ' is the effective coefficient of friction, τ is the shear stress and σ is the fault-normal stress

297 (+ve for fault clamping) [Byerlee, 1978]. During coseismic slip the shear stress drops by $\Delta\tau_c$, whilst
 298 the normal stress change $\Delta\sigma_c$ is negligible. In order for the fault to reach its failure condition again
 299 following postseismic stress changes $\Delta\tau_p$ and $\Delta\sigma_p$ requires the following condition to be satisfied:

$$\underbrace{\frac{\Delta\tau_p}{\Delta\tau_c} - \mu' \left(\frac{\Delta\sigma_p}{\Delta\tau_c} \right)}_{\text{Stress Changes}} + \underbrace{\Delta\mu' \left(\frac{\sigma}{\Delta\tau_c} \right)}_{\text{Strength Changes}} \simeq 1, \quad (1)$$

300 assuming that $\Delta\sigma_p \ll \sigma$ (see Supplementary Text S2 for derivation). Equation 1 shows that the stress
 301 changes on the fault are primarily a product of two effects: the postseismic shear stress change relative
 302 to the coseismic shear stress drop $\Delta\tau_p/\Delta\tau_c$ (the ‘shear stress recovery’) and the postseismic change in
 303 fault-normal stress relative to the coseismic shear stress drop $\Delta\sigma_p/\Delta\tau_c$ (the ‘fault clamping’). Changes
 304 in the frictional strength of the fault surface $\Delta\mu'$ may also contribute by reducing the fault stress needed
 305 for failure (the ‘strength change’ term in Equation 1). We evaluate the terms $\Delta\tau_p/\Delta\tau_c$ and $\Delta\sigma_p/\Delta\tau_c$
 306 from our numerical models, and not the more common metric of Coulomb stress ($\Delta\tau_p - \mu'\Delta\sigma_p$), to
 307 explicitly separate reloading due to changes in fault stress from the effects of fault strength. From this
 308 analysis, we can isolate the size of the strength change term, which we discuss in detail in Section 4.

309 We calculated $\Delta\tau_c$, $\Delta\tau_p$ and $\Delta\sigma_p$ using the Computational Infrastructure for Geodynamics code
 310 RELAX, which solves for the quasi-static deformation in elastic and visco-elastic media in response
 311 to fault slip using an equivalent body-force approach [see Barbot et al., 2009; Barbot and Fialko,
 312 2010b,a]. We used a 102 km-wide domain with a discretisation of 0.2 km to ensure that models
 313 accurately resolved the gradients in strain and stress near the edges of the coseismic rupture. Fault
 314 slip was also tapered at the margins of each fault patch to dampen stress singularities. The boundaries
 315 of the model domain were set to be at least $5L$ (~ 50 km) away, so that the periodicity in the solutions
 316 for displacement and stress introduced by the discrete Fourier transform that RELAX uses had little
 317 effect on the model results. After calculating the coseismic stress changes for the given coseismic slip
 318 distribution, the models were run for 5 relaxation times to approximate the fully-relaxed state.

319 3.1.1 Results of the Generalised Modelling

320 We ran nine sets of forward calculations, varying the deformation mechanism (visco-elastic only,
 321 afterslip only and coupled afterslip + visco-elastic), the coseismic fault slip u , the depth of the coseismic
 322 rupture relative to the elastic layer thickness z_r/z_e and the along-strike length of the coseismic rupture
 323 L . We found that varying the along-strike length of fault that is able to slide through afterslip L_f had

324 little effect on the estimates of fault reloading when $L_f > 5$ km (Supplementary Figure 5), therefore we
325 fixed L_f to 5 km in all models. All other parameters, such as the elastic properties of the seismogenic
326 layer, were held constant. The results of the modelling, expressed in terms of shear stress recovery
327 $\Delta\tau_p/\Delta\tau_c$, are shown in Figure 7. The equivalent results for the fault clamping $\Delta\sigma_p/\Delta\tau_c$ are shown in
328 Supplementary Figure 6, but are not discussed further in the main text as they make a relatively minor
329 ($\ll 5\%$) contribution to the reloading when scaled by the effective friction μ' on earthquake-generating
330 faults (0.01–0.4; see Toda et al. [2011]; Copley et al. [2018]; Collettini et al. [2019]).

331 Models that only allow stress changes to be relaxed through viscous flow beneath the elastic layer
332 consistently show that the shear stress recovery is largest at the base of the elastic layer and decreases
333 non-linearly towards the surface (Figure 7a-c). Shear stress recovery is also largest within the centre
334 of the rupture, and smallest along its edges. These first-order patterns are a result of the postseismic
335 strain within the elastic layer being largest at its base, where the coseismic stress changes are largest
336 and will have driven the most viscous flow. The postseismic strains and stress changes decay into the
337 elastic layer, as the layer resists deformation from viscous flow below. Varying the amount of fault slip
338 has no effect on the shear stress recovery, and varying the rupture length has only a small effect on shear
339 stress recovery. Changing the fault slip does not alter the shear stress recovery because increasing fault
340 slip causes a proportional increase in the amount of viscous flow needed to relax the coseismic stress
341 change, and therefore a proportional amount of fault reloading. The depth of the rupture relative to
342 the elastic layer thickness is the dominant control on the fault reloading, with shear stress recovery
343 increasing significantly as the rupture depth approaches the elastic layer thickness. Nevertheless, even
344 when the fault ruptures to the base of the elastic layer, the shear stress recovery remains less than
345 40% of the coseismic stress drop at the base of the rupture, and less than 10% at the surface.

346 Models that only allow stress changes to be relaxed through afterslip show a different pattern of
347 reloading (Figure 7d-f). Shear stress recovery is largest along the edges of the coseismic rupture
348 and within the shallowest part of the elastic layer. Again, the shear stress recovery is independent
349 of the amount of coseismic slip, but does depend on the down-dip extent of the coseismic rupture
350 relative to the elastic layer thickness and the along-strike length of the rupture area. These patterns
351 indicate that the larger the area that surrounds the rupture that is able to slip in response to coseismic
352 stress changes, the more this area is able to slide postseismically before elastic resistance from the
353 surrounding rocks balances the stresses driving slip. Afterslip only leads to a shear stress recovery of
354 $< 30\%$ of the coseismic stress drop on any particular part of the rupture.

355 Models that include mechanically-coupled afterslip and visco-elastic relaxation generate the largest

356 shear stress recovery on the rupture area (Figure 7g-i). Viscous flow can load the base of the coseismic
357 rupture whilst afterslip can load the edges and top of the rupture. Shear stress recovery of 45% the
358 coseismic stress drop occurs along the edges of the rupture, whilst in the shallow part of the elastic
359 layer the maximum shear stress recovery is 20%.

360 These calculations demonstrate that postseismic relaxation around the margins of a $\sim M_w$ 6 rupture
361 can only partly reload the rupture area. Variations in the depth of the coseismic rupture relative to
362 the thickness of the seismogenic layer, the area of the rupture and afterslip region, and the deformation
363 mechanisms that contribute to postseismic relaxation, will all influence the shear stress recovery, but
364 these cannot increase the shear stress recovery beyond 45%. This result is perhaps unsurprising, given
365 that most faults rupture after hundreds to thousands of years without an earthquake, which indicates
366 that slow interseismic strain accumulation makes up the remainder of the stress deficit on most active
367 faults. In the next section, we apply these models to the Mochiyama earthquakes and compare them
368 with the observed surface deformation.

369 **3.2 Specific Models of Stress Changes on the Mochiyama Fault**

370 To model the stress changes specific to the Mochiyama earthquake sequence, we used the slip distribu-
371 tion of Fukushima et al. [2018] projected onto a planar approximation of the Mochiyama Fault with the
372 geometry defined by the relocated seismicity and surface ruptures. In Section 2, we showed that the
373 slip model of Fukushima et al. [2018] overestimates the amount of coseismic moment release and deep
374 slip on the southern portion of the fault, but otherwise the general distribution of slip is likely to be
375 accurate given that it matches the along-strike length and across-strike width of the LOS displacement
376 pattern measured by InSAR. We therefore scaled the amount of slip such that it matches the moment
377 release calculated from body-waveform modelling and the coseismic strain from GPS measurements
378 in our reference calculations. With this modification, the slip distribution has a peak slip of 0.7 m, an
379 average shear stress drop $\Delta\tau_c$ of 3.5 MPa and a peak shear stress drop of 9 MPa in the centre of the
380 rupture (Supplementary Figure 7). We then explore how uncertainties in the slip distribution could
381 effect the estimates of fault reloading later in this section.

382 We calculated the postseismic reloading of the rupture area by allowing the coseismic stress changes to
383 be relaxed by afterslip on the mainshock fault plane around the margins of the rupture, which spans
384 the area that experienced normal-faulting aftershocks with nodal planes parallel to the mainshock
385 (from Figure 5a,b). Coseismic stress changes below 10 km are either relaxed by distributed viscous

386 flow, or by localised shear in a shear zone that follows the down-dip projection of the mainshock fault
387 plane. The depth of the transition in deformation mechanism was chosen on the basis of the sharp
388 cut-off in microseismicity at 10 km depth (Supplementary Figure 4).

389 The predicted deformation is highly localised around the fault, and only the strain measured by GPS
390 triangles that span the fault, or are just to the south-west of the fault trace in the immediate fault
391 hangingwall, show strain amplitudes larger than the measurement uncertainty (0.2–0.3 microstrain).
392 We therefore focus on comparing the modelled and observed deformation in these triangles.

393 Models that both include, and exclude, distributed viscous flow at depths >10 km can match the
394 observed pattern of postseismic strain during the inter-event period, with ENE-WSW extension in
395 triangles that span the Mochiyama Fault. One of the key differences between the models is that deep
396 viscous flow generates more across-fault extension (2.0 microstrain) than if only afterslip and localised
397 viscous shear are allowed to relax the coseismic stress changes (0.8 microstrain). This difference reflects
398 the fact that distributed flow at depth produces long-wavelength surface deformation that strongly
399 affects the GPS sites that are 10–20 km from the fault. Nevertheless, both models still significantly
400 under-estimate the total amount of inter-event extension observed across the Mochiyama Fault (3.1–
401 3.6 microstrain). GPS triangles to the south-west of the fault trace within the fault hangingwall show
402 different patterns of strain for the different mechanisms of postseismic relaxation at depth. Afterslip
403 beneath the rupture produces a small amount of incremental NE-SW extension, whilst distributed
404 viscous flow produces incremental contraction that rotates in orientation from north to south that is
405 more consistent with the observed inter-event strain (Figure 8a,b).

406 Despite the differences in the predicted surface strain, the models yield similar patterns of afterslip
407 and fault reloading, with up to 80% shear stress recovery along the margins of the rupture and less
408 than 10% within its interior (Figure 8c,d). The shear stress recovery along the margins of the rupture
409 area is larger than in the spatially-uniform slip models shown in Section 3.1, because the margins
410 of the rupture have a low coseismic stress drop when calculated using the distributed slip model,
411 yet experience the largest postseismic stress changes. The shear stress recovery averaged over the
412 rupture for models with and without visco-elastic relaxation are 33% and 28%, respectively, which is
413 consistent with the average shear stress recovery in the generalised models that use a similar rheological
414 structure (Figure 7e,h). As seen in the Section 3.1, viscous flow at depth has little effect on the shear
415 stress recovery, because the fault did not rupture all the way to the base of the seismogenic layer.
416 The modelled fault clamping $\Delta\sigma_p/\Delta\tau_c$ is everywhere <10% (Supplementary Figure 8), and therefore
417 makes a negligible contribution to the reloading when scaled by the effective friction.

418 3.2.1 Effects of the Coseismic Slip Distribution on Reloading

419 The stress changes that drive postseismic relaxation are a function of gradients in the input slip model.
420 Therefore, the smoothing used to regularise the inversions for coseismic slip, or the inclusion of some
421 postseismic slip in the coseismic slip distribution, may have an effect on the predicted amplitude of
422 postseismic deformation. To explore whether this effect can account for the difference between the
423 modelled and observed inter-event strain across the Mochiyama Fault, we ran a series of calculations
424 in which we artificially vary the smoothing of the input slip distribution in the 2011 earthquake by
425 removing areas with slip less than some minimum value u_{min} , and then redistribute the remaining
426 moment release evenly across the rupture area [e.g. Barbot et al., 2009]. This process leads to a
427 compaction of the slip distribution, and an increase in the coseismic stress drop (Supplementary Figure
428 4), with a slight decrease in the fit between the observed and modelled coseismic surface deformation.

429 Models with more compact slip distributions and higher stress drops cause more postseismic relaxation
430 and larger surface strains (Figure 9a). If all areas with slip <0.4 – 0.5 m are removed, which adjusts
431 the stress drop to be 10–15 MPa, then the models can account for the observed 3.1–3.6 microstrain
432 of across-fault extension over the inter-event period. Nevertheless, compacting the slip distribution
433 has little effect on the average shear stress recovery on the rupture (Figure 9b), because the coseismic
434 stress drop also increases. The generalised calculations in Section 3.1.1 provide the physical expla-
435 nation for this feature of the models: increased stress drop causes increased elastic strain within the
436 surrounding crust, which itself leads to a proportional amount of fault zone reloading through postseis-
437 mic relaxation. Therefore, although uncertainties in the roughness of the slip distribution of the 2011
438 earthquake can account for the discrepancy between the modelled and observed across-fault strain
439 between the 2011 and 2016 Mochiyama earthquakes, the rupture area can still only be reloaded by
440 on average $\lesssim 35\%$ of the coseismic stress drop through postseismic relaxation (Figure 9b). In the next
441 section, we explore what contributions the static and time-dependent stress changes from the Iwaki
442 earthquake sequence could have made to the reloading of the Mochiyama Fault.

443 3.2.2 Stress Changes from the Iwaki Earthquakes

444 We used the fault geometry and slip estimates from Fukushima et al. [2013] to calculate the co- and
445 post-seismic displacements, and the resulting stress changes on the Mochiyama Fault, due to slip in the
446 Iwaki earthquake sequence. The modelled coseismic strain matches the strain observed by the GPS
447 network, and can account for the 0.7 microstrain of extension across the Mochiyama Fault in April

448 2011 (Supplementary Figure 9). We find that the Iwaki earthquakes caused a <0.3 – 0.4 MPa increase
449 in shear stress (Figure 10b) and a <0.2 – 0.3 MPa decrease in normal stress (Figure 10c) along the
450 northern-most portion of the Mochiyama Fault. The amplitude of these static stress changes drop off
451 significantly towards the southern edge of the Mochiyama Fault, as stress decays as the inverse cube of
452 distance from the strain source in the elastic crust [Okada, 1992]. Therefore, the Iwaki earthquakes did
453 move the Mochiyama Fault closer to failure, but they contributed a shear stress recovery of <5 – 10%
454 of the coseismic stress drop (3 – 15 MPa; Figure 10a).

455 Postseismic relaxation on the Iwaki Faults could have produced up to 0.3 – 0.5 microstrain of extension
456 across the Mochiyama Fault, which is ~ 10 – 15% of the observed inter-event extension. The stress
457 changes oppose the initial static loading with a shear stress decrease of <0.2 – 0.3 MPa (Figure 10d)
458 and a normal stress increase of <0.3 – 0.4 MPa (Figure 10e) along the base of the Mochiyama Fault.
459 Models that do not include distributed viscous flow below 10 km depth predict negligible strain and
460 stress changes on the Mochiyama Fault that are $\ll 0.1$ MPa (Supplementary Figure 10). Mechanically-
461 coupled models that include the co- and post-seismic stress changes in both events show that the Iwaki
462 earthquakes will have only slightly inhibited afterslip on the northern half of the Mochiyama Fault,
463 and could have reduced the average shear stress recovery by $<2\%$ (Figure 10f). Therefore, despite
464 the proximity of the Iwaki earthquakes to Mochiyama, the static and time-dependent stress changes
465 caused by the Iwaki earthquake sequence played a minor role in the reloading the Mochiyama Fault.

466 3.2.3 Stress Changes from the Tohoku-oki Earthquake

467 Coseismic slip in the 11th March 2011 Tohoku-oki earthquake stretched the overriding plate and
468 caused widespread changes in the style and frequency of seismicity in the shallow crust of mainland
469 Japan [Okada et al., 2011]. Seismicity in North Kanto prior to the Tohoku-oki earthquake consisted
470 solely of normal faulting [Imanishi et al., 2012], and the static stress changes from the Tohoku-oki
471 earthquake were equivalent to a shear stress increase of 0.8 MPa and a normal stress drop of -1.2 MPa
472 on the Mochiyama Fault (calculated from the model of Hu et al. [2016]). These stress changes did
473 not immediately trigger rupture, but likely brought the Mochiyama Fault close to failure. Postseismic
474 relaxation following the Tohoku-oki earthquake contributed additional loading of faults in mainland
475 Japan [Becker et al., 2018]. Fukushima et al. [2018] calculated that afterslip on the megathrust around
476 the Tohoku-oki rupture area would have subject the Mochiyama Fault to an increase in shear stress
477 of 0.1 MPa and a decrease in fault normal stress of -0.2 MPa over the period March 2011 to December
478 2016. A more complex calculation by Hu et al. [2016], which includes the effects of visco-elastic

479 relaxation beneath the crust, afterslip on the megathrust, and interseismic relocking of the subduction
480 interface, suggests there may have been a shear stress increase of 0.07 MPa and a normal stress
481 drop of -0.2 MPa on the Mochiyama Fault over the same period (Supplementary Figure 10). Both
482 models predict stress changes that are small compared to the coseismic stress drop in the Mochiyama
483 earthquake, and would directly contribute to $\ll 5\%$ of the shear stress recovery on the rupture area.

484 The stress changes from the Tohoku-oki earthquake will have influenced the postseismic afterslip
485 around the rupture area on the Mochiyama Fault [Fukushima et al., 2018]. We ran models that include
486 the relaxation of both the coseismic stress changes due to the Mochiyama earthquake through localised
487 afterslip, and the co- and post-seismic stress changes from the Tohoku-oki earthquake resolved on the
488 Mochiyama Fault. We include the coseismic stress changes from the Tohoku-oki earthquake, as it is
489 unlikely that a significant fraction of this stress imposed on the Mochiyama Fault was relaxed by the
490 timing of the 2011 Mochiyama earthquake given that they were only 7 days apart. These calculations
491 produce up to 3.0 microstrain of extension across the Mochiyama Fault by boosting the average
492 amount of afterslip around the rupture area from ~ 20 cm to ~ 60 cm. Notably the orientations of
493 the modelled minimum principal strain axes in triangles that span the fault are rotated anti-clockwise
494 relative to strain axes measured by the GPS network. The relaxation of stress changes caused by the
495 Tohoku-oki earthquake by slip on the Mochiyama Fault can therefore account for the amplitude of the
496 extension measured by the GPS network over the inter-event period (Figure 11a). This afterslip must
497 be mostly restricted to shallower than ~ 5 km, otherwise the models predict extensional strain within
498 GPS triangles in the hangingwall of the Mochiyama Fault, which does not match the observation of
499 contractional strain in these triangles (Figure 11b,c). With the additional afterslip, the average shear
500 stress recovery on the mainshock rupture area increases to 40%, which is still only a fraction of that
501 needed to entirely reload the rupture to its former failure stress.

502 4 Discussion

503 4.1 Surface Strain and Stress Changes on the Mochiyama Fault

504 Our modelling demonstrates that postseismic relaxation driven by coseismic stress changes can account
505 for the pattern and amplitude of the strain across the Mochiyama Fault if the stress drop within the
506 earthquake was 10–15 MPa and all of the coseismic stress changes were relaxed by creep and viscous
507 flow in the inter-event period. Such a stress drop would require average differential stresses within the

508 top 10 km of the crust of at least 20–30 MPa. It is unlikely the differential stresses exceed a few tens of
509 MPa, given the widespread change in the mechanisms of earthquakes in mainland Japan following the
510 relatively minor ($<1\text{--}2$ MPa) stress changes caused by the Tohoku-oki earthquake [Wang et al., 2019].
511 As the stress changes on the rupture area of the Mochiyama Fault caused by postseismic relaxation
512 are proportional to the coseismic stress drop, a higher stress drop does not equate to a higher shear
513 stress recovery. Therefore, models that match the observed inter-event strain solely through local
514 postseismic relaxation recover only 35% of the fault-averaged coseismic shear stress drop, or less.

515 The static stress changes due to the nearby Iwaki earthquakes moved the Mochiyama Fault closer
516 to failure, but recovered only $<10\%$ of the stress drop in the 2011 Mochiyama earthquake. Sub-
517 sequent postseismic relaxation will have unloaded the Mochiyama Fault and moved it further from
518 failure. Therefore the stress changes caused by nearby earthquakes had a small effect on reloading the
519 Mochiyama Fault in comparison to the localised postseismic relaxation around the coseismic rupture.

520 The Tohoku-oki earthquake, and its postseismic deformation, boosted the amount of afterslip on the
521 Mochiyama Fault and brought the rupture area closer to failure. Models that include these effects can
522 account for the amplitude of the measured across-fault extension in the inter-event period, but only
523 produce a shear stress recovery on the Mochiyama Fault of 40% or less. Considering the effects of the
524 Tohoku-oki earthquake on the postseismic relaxation around the Mochiyama Fault can account for
525 the order of magnitude difference in the amplitude of the across-fault extension observed following the
526 2011 and 2016 Mochiyama earthquakes. However, the inference of Fukushima et al. [2018] that this
527 additional afterslip on the Mochiyama Fault reloaded it back to its former failure stress is inconsistent
528 with our model results. We instead find that the rupture area on the Mochiyama Fault could only have
529 been reloaded by less than half of the coseismic shear stress drop by the time of the 2016 earthquake.

530 In summary, the observed inter-event strain across the Mochiyama Fault measured by the GPS network
531 can be accounted for by either localised postseismic relaxation of coseismic stress changes following
532 a fault-averaged stress drop of 10–15 MPa, or by the relaxation of both coseismic stress changes and
533 the stresses caused by the Tohoku-oki earthquake following a fault-averaged stress drop of 3–4 MPa.
534 However, neither of these mechanisms can have recovered more than 35–50% of the coseismic stress
535 drop averaged over the rupture area. We therefore conclude that the stresses needed to break the
536 Mochiyama Fault in earthquakes must have decreased through time to account for the short inter-
537 event time between the 2011 and 2016 earthquakes by at least 2–10 MPa (Figure 12).

4.2 Time-Dependent Decrease in Fault Strength

Most active faults do not experience such short inter-event times between moderate-magnitude earthquakes, suggesting that the mechanisms decreased the strength of the Mochiyama Fault between 2011 and 2016 were unusual. The static strength of the fault’s surface can be described by the effective frictional resistance to slip $\mu' = \mu(1 - \lambda)$, where μ is the intrinsic friction and $\lambda = P_f/\sigma$ where P_f is the pore-fluid pressure on the fault [Hubbert and Rubey, 1959]. The drop in fault strength may therefore have been due to a decrease in the intrinsic friction of the material making up the fault surface, or an increase in the pore-fluid pressure within the fault core.

Vertical migration of high-pressure fluids through the shallow crust in mainland Japan following the Tohoku-oki earthquake has been widely invoked to account for migrating seismicity [Yoshida et al., 2015, 2017, 2020], temporal changes in the shallow shear-wave velocity structure [Wang et al., 2021] and groundwater geochemistry around crustal faults [Sato et al., 2020]. Infiltration of fluid onto the rupture area of the Mochiyama Fault could therefore have reduced the average shear stresses needed for failure, whilst also promoting aftershock seismicity, by changing the effective fault-normal stresses [Hainzl, 2004]. We did not find any evidence for the spatial migration of earthquake hypocentres around the Mochiyama Fault that might reflect a front of highly-pressurised fluid causing small patches of the fault to fail sequentially (Supplementary Figure 12) [e.g. Shapiro et al., 1997; Walters et al., 2018]. Any fluid infiltration onto the fault zone also did not affect the time-scale over which coseismic stress changes were relaxed, as the postseismic transients after the 2011 and 2016 Mochiyama earthquakes followed similar temporal decays. Therefore the mechanism that decreased the strength of the Mochiyama Fault had surprisingly little effect on the geodetic or microseismic observations, other than the highly energetic aftershock sequence beneath the mainshock rupture area (see Section 2.4).

5 Conclusion

We have demonstrated that earthquake-related stress changes and their postseismic relaxation can explain the pattern of strain measured by Japan’s GPS network during the 2011–2016 Mochiyama earthquake sequence in North Kanto. Models that match the observed inter-event strain can only reload the rupture area on the fault by less than 35–50% of the fault-averaged coseismic stress drop, irrespective of the rheological structure of the crust and mantle in North Kanto, or the mechanisms of postseismic relaxation. We conclude that the Mochiyama Fault experienced a drop in its effec-

567 tive strength, and the shear stresses needed to break the fault reduced by at least 2–10 MPa. The
568 mechanism(s) that caused this weakening are unclear, but appear to have been associated with an
569 unusually energetic aftershock sequence around the margins of the coseismic rupture. Time-dependent
570 changes in fault strength may therefore play a role in modulating the timing of moderate-magnitude
571 earthquakes, but may be difficult to detect using geodetic and microseismicity observations.

572 **Acknowledgements**

573 SW was supported by the Denman Baynes Junior Research Fellowship at Clare College, University of
574 Cambridge. Part of this work was completed during NF's M.Sci thesis at the University of Cambridge.
575 This work was partly supported by COMET – the NERC Centre for the Observation and Modelling
576 of Earthquakes, Volcanoes, and Tectonics, a partnership between UK universities and the BGS. Both
577 SW and NF contributed equally to this article. The authors thank Dr. Yo Fukushima, Dr. Takahiko
578 Uchide, Dr. Keitaro Komura and Dr. Yan Hu for swiftly providing data from their publications.

579 **Data Availability**

580 All data and code used in this study are freely available online. The GPS data used in this study are
581 available from http://datahouse1.gsi.go.jp/terras/terras_english.html (last accessed March
582 2020). The JMA microseismicity data are available from [https://www.data.jma.go.jp/svd/eqev/
583 data/bulletin/index_e.html](https://www.data.jma.go.jp/svd/eqev/data/bulletin/index_e.html) (last accessed March 2021) and the NIED earthquake moment tensors
584 are available from <https://www.fnet.bosai.go.jp/fnet/event/search.php> (last accessed March
585 2021). The Envisat and Sentinel-1 data are freely accessible through ESAs Copernicus SchiHub [https:
586 //scihub.copernicus.eu/](https://scihub.copernicus.eu/) (last accessed January 2022). The numerical model RELAX is available
587 from <https://geodynamics.org/cig/software/relax/> (last accessed March 2021).

References

- Bagge, M. and Hampel, A. (2017). Postseismic Coulomb stress changes on intra-continental dip-slip faults due to viscoelastic relaxation in the lower crust and lithospheric mantle: insights from 3D finite-element modelling. *International Journal of Earth Sciences*, 106(8):2895–2914.
- Barbot, S. and Fialko, Y. (2010a). A unified continuum representation of post-seismic relaxation mechanisms: semi-analytic models of afterslip, poroelastic rebound and viscoelastic flow. *Geophysical Journal International*, 182(3):1124–1140.
- Barbot, S. and Fialko, Y. (2010b). Fourier-domain Green’s function for an elastic semi-infinite solid under gravity, with applications to earthquake and volcano deformation. *Geophysical Journal International*, 182(2):568–582.
- Barbot, S., Fialko, Y., and Bock, Y. (2009). Postseismic deformation due to the Mw 6.0 2004 Parkfield earthquake: Stress-driven creep on a fault with spatially variable rate-and-state friction parameters. *Journal of Geophysical Research: Solid Earth*, 114(B7):B07405.
- Becker, T. W., Hashima, A., Freed, A. M., and Sato, H. (2018). Stress change before and after the 2011 M9 Tohoku-oki earthquake. *Earth and Planetary Science Letters*, 504:174–184.
- Bedford, J. R., Moreno, M., Deng, Z., Oncken, O., Schurr, B., John, T., Báez, J. C., and Bevis, M. (2020). Months-long thousand-kilometre-scale wobbling before great subduction earthquakes. *Nature*, 580(7805):628–635.
- Bourne, S. J., Árnadóttir, T., Beavan, J., Darby, D. J., England, P. C., Parsons, B., Walcott, R. I., and Wood, P. R. (1998). Crustal deformation of the Marlborough Fault Zone in the South Island of New Zealand: Geodetic constraints over the interval 1982-1994. *Journal of Geophysical Research: Solid Earth*, 103(B12):30147–30165.
- Byerlee, J. (1978). Friction of rocks. *Pure and Applied Geophysics*, 116(4-5):615–626.
- Cheloni, D., D’Agostino, N., D’Anastasio, E., Avallone, A., Mantenuto, S., Giuliani, R., Mattone, M., Calcaterra, S., Gambino, P., Dominici, D., Radicioni, F., and Fastellini, G. (2010). Coseismic and initial post-seismic slip of the 2009 Mw 6.3 L’Aquila earthquake, Italy, from GPS measurements. *Geophysical Journal International*, 181(3):1539–1546.
- Churchill, R. M., Werner, M. J., Biggs, J., and Fagereng, Å. (2022). Afterslip Moment Scaling and Variability From a Global Compilation of Estimates. *Journal of Geophysical Research: Solid Earth*, 127(4):e2021JB023897.

- Collettini, C., Tesei, T., Scuderi, M. M., Carpenter, B. M., and Viti, C. (2019). Beyond Byerlee friction, weak faults and implications for slip behavior. *Earth and Planetary Science Letters*, 519:245–263.
- Copley, A., Grützner, C., Howell, A., Jackson, J., Penney, C., and Wimpenny, S. (2018). Unexpected earthquake hazard revealed by Holocene rupture on the Kenchreai Fault (central Greece): Implications for weak sub-fault shear zones. *Earth and Planetary Science Letters*, 486:141–154.
- Ekström, G., Nettles, M., and Dziewoński, A. (2012). The global CMT project 2004–2010: Centroid-moment tensors for 13,017 earthquakes. *Physics of the Earth and Planetary Interiors*, 200:1–9.
- Ellis, S. and Stöckhert, B. (2004). Elevated stresses and creep rates beneath the brittle-ductile transition caused by seismic faulting in the upper crust. *Journal of Geophysical Research: Solid Earth*, 109(5).
- Farr, T. G., Rosen, P. A., Caro, E., Crippen, R., Duren, R., Hensley, S., Kobrick, M., Paller, M., Rodriguez, E., Roth, L., Seal, D., Shaffer, S., Shimada, J., Umland, J., Werner, M., Oskin, M., Burbank, D., and Alsdorf, D. (2007). The Shuttle Radar Topography Mission. *Reviews of Geophysics*, 45(2):RG2004.
- Freed, A. M. (2005). Earthquake Triggering by Static, Dynamic and Postseismic Stress Transfer. *Annual Review of Earth and Planetary Sciences*, 33(1):335–367.
- Freed, A. M. and Lin, J. (1998). Time-dependent changes in failure stress following thrust earthquakes. *Journal of Geophysical Research: Solid Earth*, 103(10):24393–24409.
- Fukushima, Y., Takada, Y., and Hashimoto, M. (2013). Complex ruptures of the 11 April 2011 Mw 6.6 Iwaki earthquake triggered by the 11 March 2011 Mw 9.0 Tohoku earthquake, Japan. *Bulletin of the Seismological Society of America*, 103(2 B):1572–1583.
- Fukushima, Y., Toda, S., Miura, S., Ishimura, D., Fukuda, J., Demachi, T., and Tachibana, K. (2018). Extremely early recurrence of intraplate fault rupture following the Tohoku-Oki earthquake. *Nature Geoscience*, 11(10):777–781.
- Hainzl, S. (2004). Seismicity patterns of earthquake swarms due to fluid intrusion and stress triggering. *Geophysical Journal International*, 159(3):1090–1096.
- Hayes, G. P. (2017). The finite, kinematic rupture properties of great-sized earthquakes since 1990. *Earth and Planetary Science Letters*, 468(June 2016):94–100.

- Hu, Y., Bürgmann, R., Uchida, N., Banerjee, P., and Freymueller, J. T. (2016). Stress-driven relaxation of heterogeneous upper mantle and time-dependent afterslip following the 2011 Tohoku earthquake. *Journal of Geophysical Research: Solid Earth*, 121(1):385–411.
- Hubbert, M. K. and Rubey, W. W. (1959). Mechanics of fluid-filled porous solids and its application to overthrust faulting. *Bulletin of the Geological Society of America*, 70(2):115–166.
- Imanishi, K., Ando, R., and Kuwahara, Y. (2012). Unusual shallow normal-faulting earthquake sequence in compressional northeast Japan activated after the 2011 off the Pacific coast of Tohoku earthquake. *Geophysical Research Letters*, 39(9).
- Kagan, Y. Y., Jackson, D. D., and Geller, R. J. (2012). Characteristic earthquake model, 1884-2011, R.I.P.
- Kato, A., Sakai, S., and Obara, K. (2011). A normal-faulting seismic sequence triggered by the 2011 off the Pacific coast of Tohoku Earthquake: Wholesale stress regime changes in the upper plate. *Earth, Planets and Space*, 63(7):745–748.
- King, G. C. P., Stein, R. S., and Lin, J. (1994). Static stress changes and the triggering of earthquakes. *Bulletin of the Seismological Society of America*, 84(3):935–953.
- Komura, K., Aiyama, K., Nagata, T., Sato, H. P., Yamada, A., and Aoyagi, Y. (2019). Surface rupture and characteristics of a fault associated with the 2011 and 2016 earthquakes in the southern Abukuma Mountains, northeastern Japan, triggered by the Tohoku-Oki earthquake. *Earth, Planets and Space*, 71(1):1–23.
- McCaffrey, R. and Abers, G. (1988). Syn3: a program for inversion of teleseismic body waveforms on microcomputers.
- Murray, J. and Segall, P. (2002). Testing time-predictable earthquake recurrence by direct measurement of strain accumulation and release. *Nature*, 419(6904):287–291.
- Nabalek, J. (1984). *Determination of earthquake source parameters from inversion of body waves*. PhD thesis, Massachusetts Institute of Technology.
- Okada, T., Yoshida, K., Ueki, S., Nakajima, J., Uchida, N., Matsuzawa, T., Umino, N., and Hasegawa, A. (2011). Shallow inland earthquakes in NE Japan possibly triggered by the 2011 off the Pacific coast of Tohoku Earthquake. *Earth, Planets and Space*, 63(7):749–754.
- Okada, Y. (1992). Internal deformation due to shear and tensile faults in a half-space. *Bulletin of the Seismological Society of America*, 82(2):1018–1040.

- Ozawa, S., Nishimura, T., Suito, H., Kobayashi, T., Tobita, M., and Imakiire, T. (2011). Coseismic and postseismic slip of the 2011 magnitude-9 Tohoku-Oki earthquake. *Nature*, 475(7356):373–376.
- Reid, H. F. (1910). The Mechanics of the Earthquake, The California Earthquake of April 18, 1906. Technical report, Carnegie Institution of Washington, Washington D.C.
- Roeloffs, E. and Langbein, J. (1994). The Earthquake Prediction Experiment at Parkfield, California.
- Sato, T., Kazahaya, K., Matsumoto, N., and Takahashi, M. (2020). Deep groundwater discharge after the 2011 Mw 6.6 Iwaki earthquake, Japan. *Earth, Planets and Space*, 72(1).
- Shapiro, S. A., Huenges, E., and Borm, G. (1997). Estimating the crust permeability from fluid-injection-induced seismic emission at the KTB site. *Geophysical Journal International*, 131(2):5–8.
- Sieh, K., Natawidjaja, D. H., Meltzner, A. J., Shen, C. C., Cheng, H., Li, K. S., Suwargadi, B. W., Galetzka, J., Philibosian, B., and Edwards, R. L. (2008). Earthquake supercycles inferred from sea-level changes recorded in the corals of west Sumatra. *Science*, 322(5908):1674–1678.
- Taymaz, T., Jackson, J. A., and Westaway, R. (1990). Earthquake mechanisms in the Hellenic Trench near Crete. *Geophysical Journal International*, 102(3):695–731.
- Toda, S., Stein, R. S., Sevilgen, V., and Lin, J. (2011). Coulomb 3.3 Graphic-rich deformation and stress-change software for earthquake, tectonic, and volcano research and teaching-user guide. *Open-File Report*.
- Toda, S. and Tsutsumi, H. (2013). Simultaneous reactivation of two, subparallel, inland normal faults during the Mw 6.6 11 April 2011 Iwaki earthquake triggered by the Mw 9.0 Tohoku-oki, Japan, Earthquake. *Bulletin of the Seismological Society of America*, 103(2 B):1584–1602.
- Uchide, T. and Imanishi, K. (2018). Underestimation of Microearthquake Size by the Magnitude Scale of the Japan Meteorological Agency: Influence on Earthquake Statistics. *Journal of Geophysical Research: Solid Earth*, 123(1):606–620.
- Waldhauser, F. and Ellsworth, W. L. (2000). A Double-difference Earthquake location algorithm: Method and application to the Northern Hayward Fault, California. *Bulletin of the Seismological Society of America*, 90(6):1353–1368.
- Walters, R. J., Gregory, L. C., Wedmore, L. N., Craig, T. J., McCaffrey, K., Wilkinson, M., Chen, J., Li, Z., Elliott, J. R., Goodall, H., Iezzi, F., Livio, F., Michetti, A. M., Roberts, G., and Vittori, E. (2018). Dual control of fault intersections on stop-start rupture in the 2016 Central Italy seismic sequence. *Earth and Planetary Science Letters*, 500:1–14.

- Wang, K., Zhu, Y., Nissen, E., and Shen, Z. K. (2021). On the Relevance of Geodetic Deformation Rates to Earthquake Potential. *Geophysical Research Letters*, 48(11):e2021GL093231.
- Wang, S., Xu, W., Xu, C., Yin, Z., Bürgmann, R., Liu, L., and Jiang, G. (2019). Changes in groundwater level possibly encourage shallow earthquakes in central Australia: The 2016 Petermann Ranges earthquake. *Geophysical Research Letters*, 46(6):3189–3198.
- Yoshida, K., Hasegawa, A., and Okada, T. (2015). Spatially heterogeneous stress field in the source area of the 2011 Mw 6.6 Fukushima-Hamadori earthquake, NE Japan, probably caused by static stress change. *Geophysical Journal International*, 201(2):1062–1071.
- Yoshida, K., Saito, T., Urata, Y., Asano, Y., and Hasegawa, A. (2017). Temporal Changes in Stress Drop, Frictional Strength, and Earthquake Size Distribution in the 2011 Yamagata-Fukushima, NE Japan, Earthquake Swarm, Caused by Fluid Migration. *Journal of Geophysical Research: Solid Earth*, 122(12):10,379–10,397.
- Yoshida, K., Uchida, N., Hiarahara, S., Nakayama, T., Matsuzawa, T., Okada, T., Matsumoto, Y., and Hasegawa, A. (2020). 2019 M6.7 Yamagata-Oki earthquake in the stress shadow of 2011 Tohoku-Oki earthquake: Was it caused by the reduction in fault strength? *Tectonophysics*, 793(August):228609.
- Zakharova, O., Hainzl, S., and Bach, C. (2013). Seismic moment ratio of aftershocks with respect to main shocks. *Journal of Geophysical Research: Solid Earth*, 118(11):5856–5864.
- Zebker, H. A. and Lu, Y. (1998). Phase unwrapping algorithms for radar interferometry: residue-cut, least-squares, and synthesis algorithms. *Journal of the Optical Society of America A*, 15(3):586.
- Zwick, P., McCaffrey, R., and Abers, G. (1994). MT5 Program.

Tables

Table 1: Parameters used in the generalised model calculations in Section 3.1.

Model Parameter	Symbol	Value
Discretisation	Δx_j	0.2 km
Number of nodes	N_j	512
Density	ρ	2800 kg/m ³
First Lamé parameter	λ	30 GPa
Shear modulus	G	30 GPa
Poisson's ratio	ν	0.2
Fault strike	θ	180°
Fault dip	δ	45°
Fault rake	ϕ	-90°

Figures

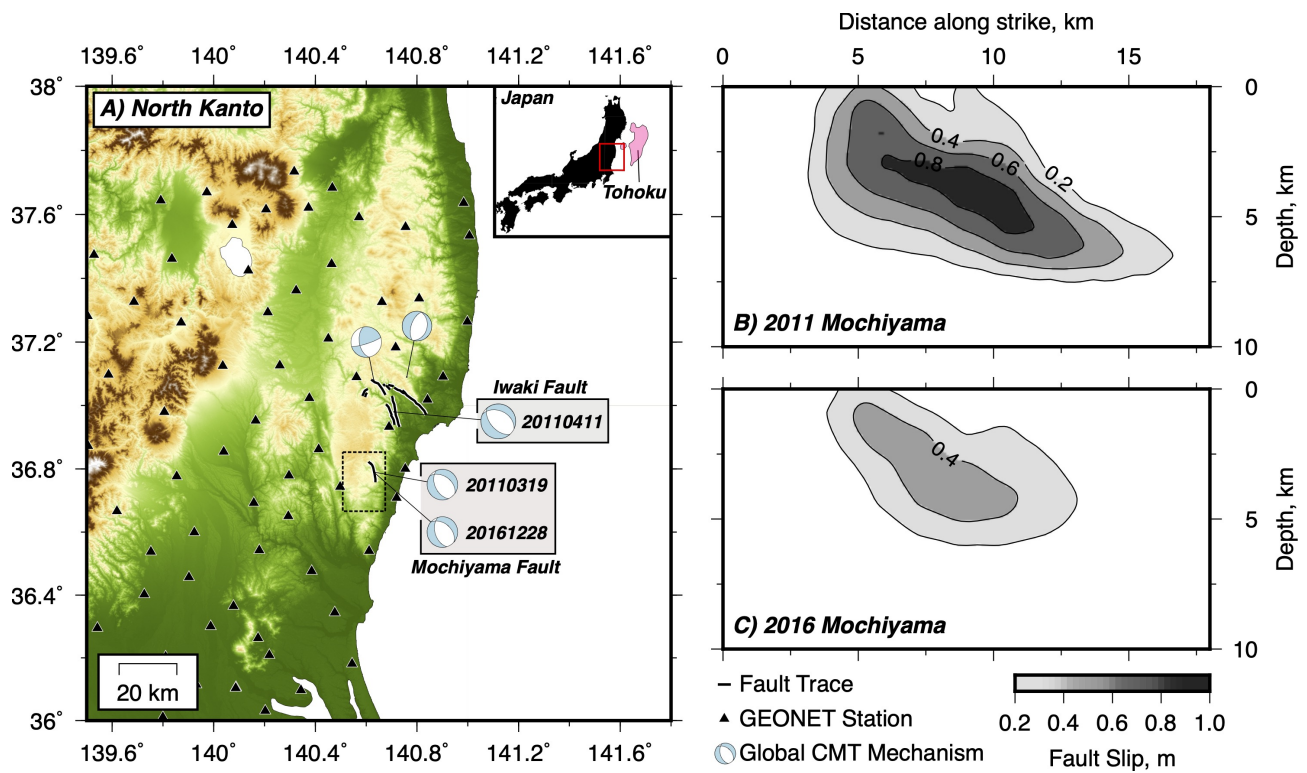


Figure 1: Overview of the North Kanto earthquake sequence. (a) Map of the North Kanto region showing the locations and Global CMT mechanisms of the Mochiyama and Iwaki earthquake sequences [Ekström et al., 2012]. GEONET GPS stations are shown as black triangles and the surface rupture traces from Toda and Tsutsumi [2013] and Komura et al. [2019] as black lines. The dashed black box is the area covered by coseismic and postseismic SAR measurements shown in Figure 4. The inset map shows the location of the North Kanto region relative to the 10 m coseismic slip contour in the M_w 9.1 11th March 2011 Tohoku-oki earthquake taken from Hayes [2017]. (b) and (c) show the slip distributions in the 2011 and 2016 Mochiyama earthquakes determined by Fukushima et al. [2018].

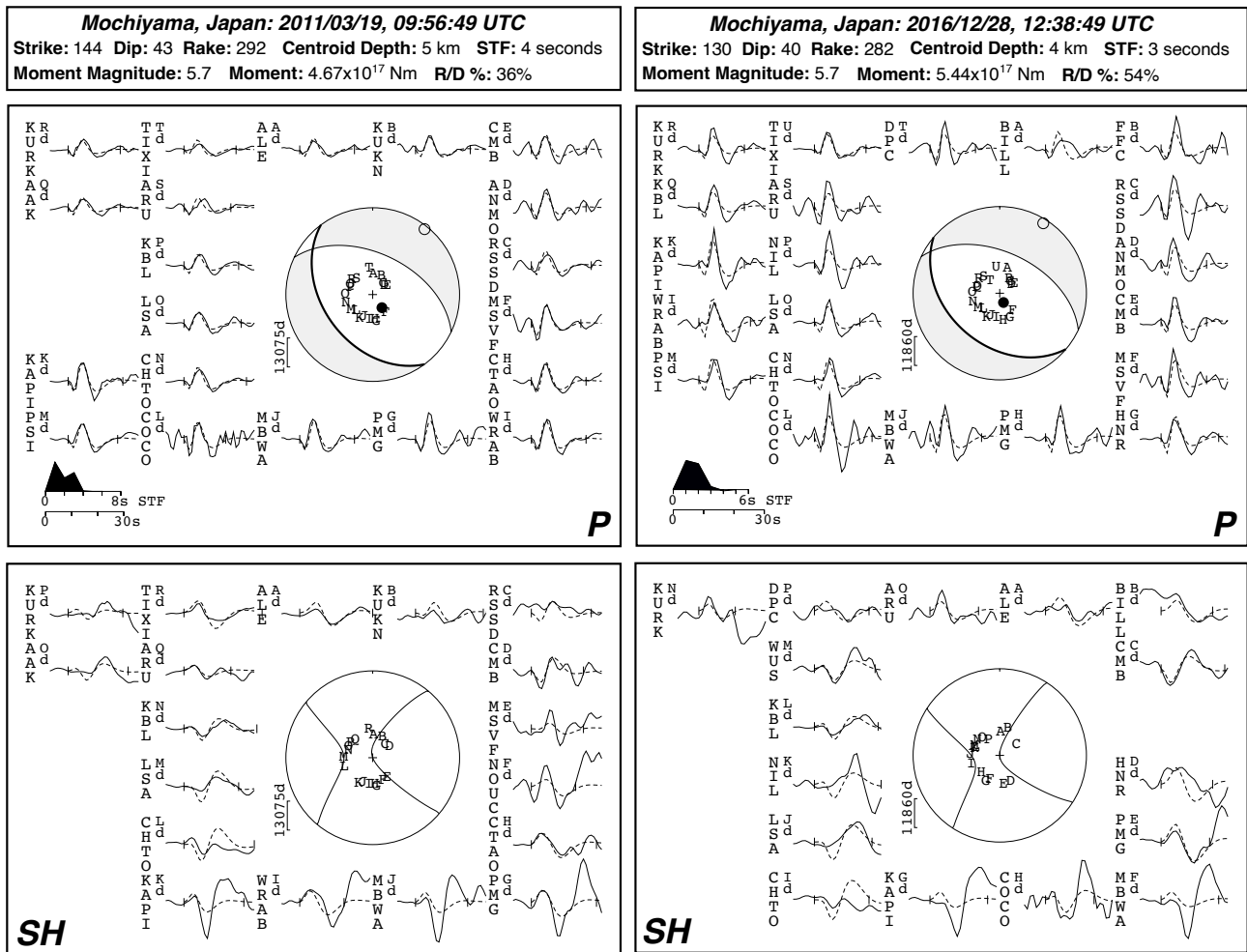


Figure 2: Minimum-misfit body-waveform models for the 2011 and 2016 Mochiyama earthquakes. The minimum-misfit parameters for each model are shown in the top panels, where STF is the source-time function and R/D% is the ratio of the residual variance to the data variance expressed as a percentage. The middle panel shows the fit between the modelled (dashed) and observed (solid) waveforms for the *P* waves. Each seismogram has to its left the three/four-letter station code, and a capital letter that corresponds to the letters plotted on the focal sphere. The source-time function and time-scale for the plotted waveforms is shown in the bottom left. The *SH* waveforms are shown in the bottom panel using the same format.

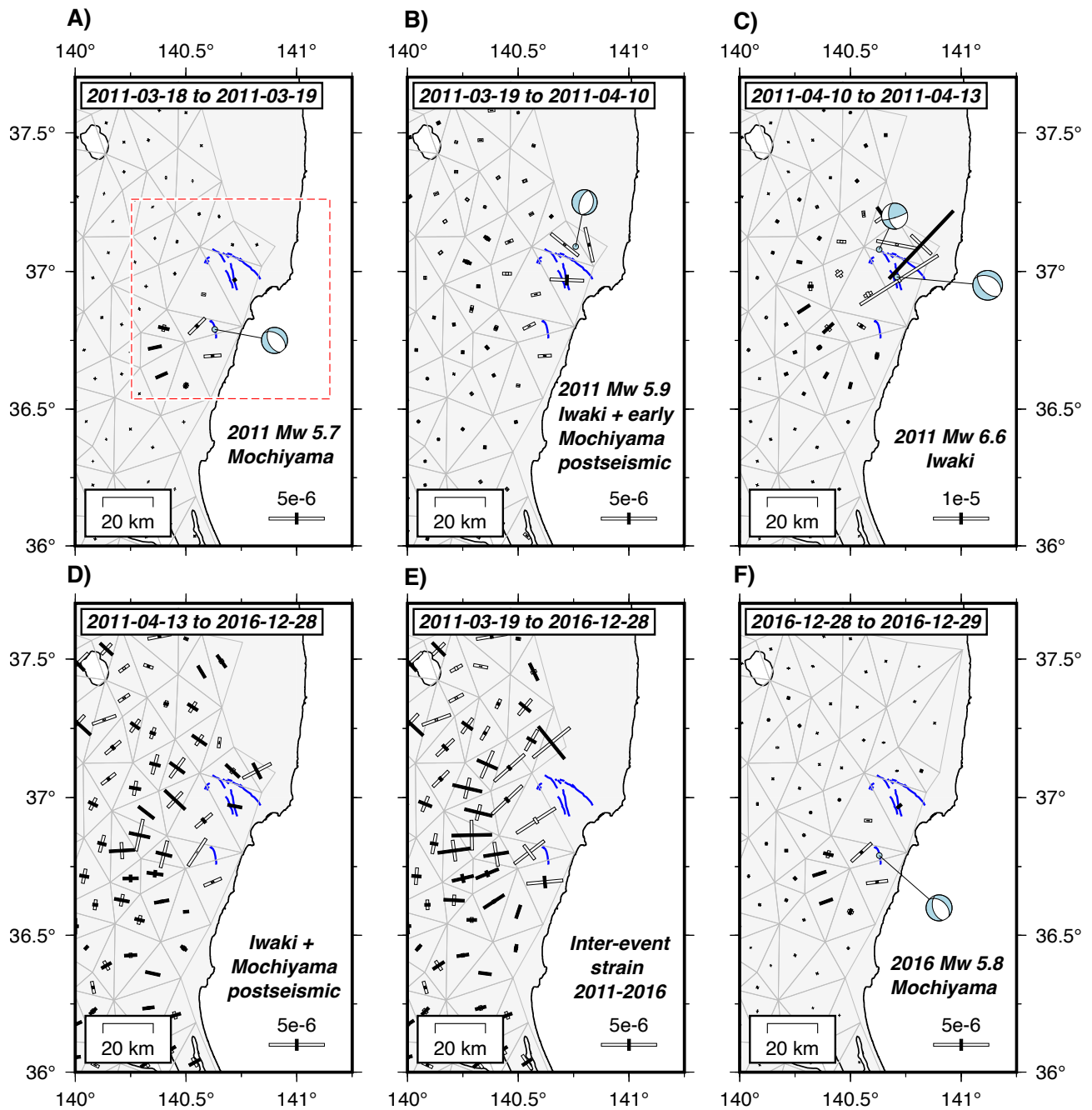


Figure 3: Incremental strain through the 2011-2016 North Kanto earthquake sequence. White bars represent principal axes of extensional strain, whilst black bars are principal axes of contractional strain. Note the difference in bar scaling between certain epochs. Blue lines are the surface traces of the Mochiyama and Iwaki Faults from Fukushima et al. [2013] and Komura et al. [2019], and the red dashed box in (a) is the map area shown in Figures 5 and 8. The GPS triangles spanning the Iwaki Fault are removed from (e) to highlight the inter-event strain across the Mochiyama Fault.

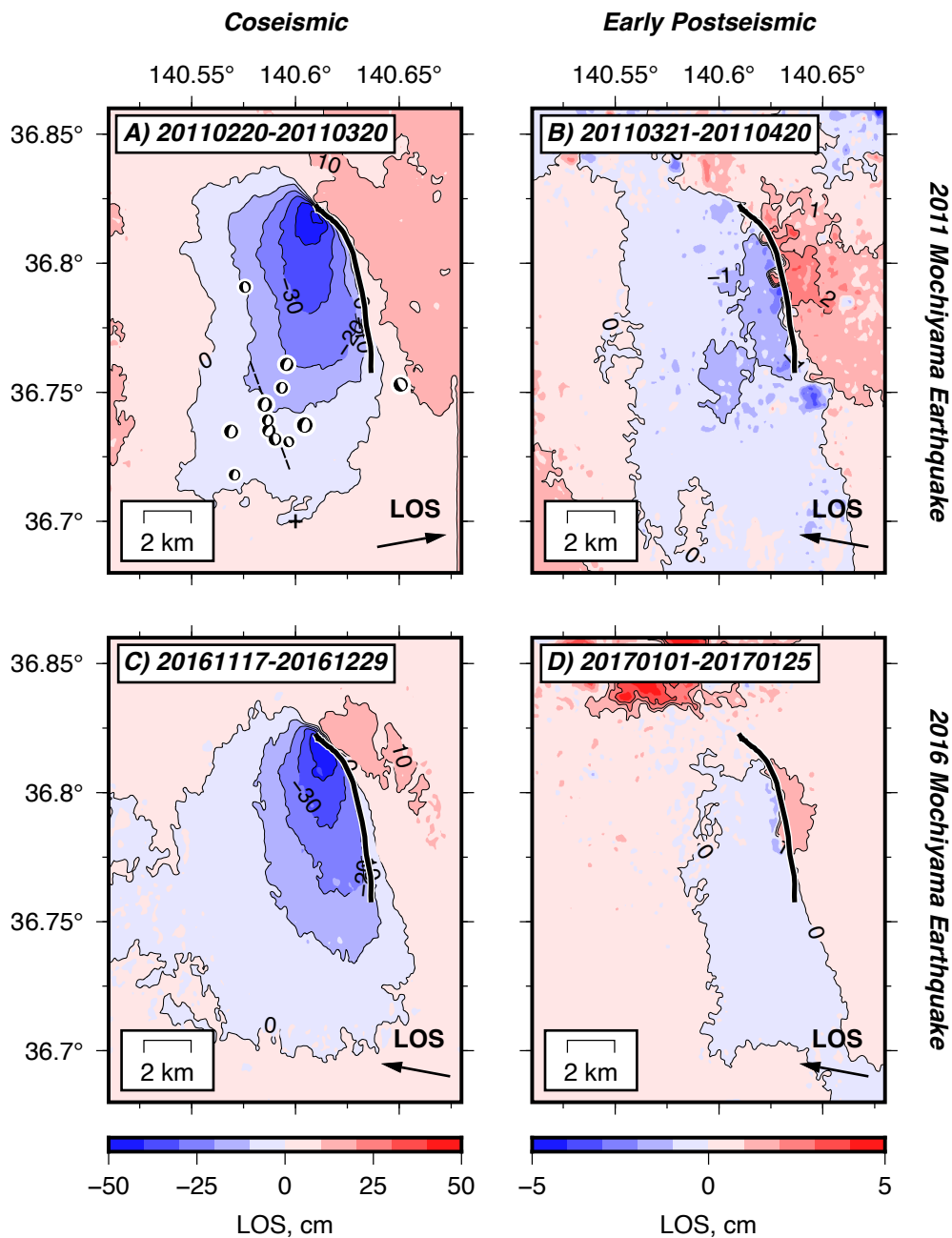


Figure 4: Coseismic and postseismic interferograms from the 2011 and 2016 earthquakes on the Mochiyama Fault. The surface trace of the fault is shown by the thick black line and the date of the primary and secondary acquisition is shown in the top left in yyymmdd format. Line-of-sight vectors are shown in the bottom right. (a) ALOS-1 ascending track coseismic interferogram showing the LOS displacement in the 19th March 2011 Mochiyama earthquake from Komura et al. [2019]. Focal mechanisms are M_w 4 and 5 foreshocks that occurred between the 11th March 2011 and 18th March 2011 from the NIED catalogue. The black-dashed line indicates the strike of the conjugate normal fault seen in the relocated microseismicity (Supplementary Figure 1). (b) Envisat descending track interferogram covering the first month of postseismic relaxation after the 2011 earthquake. (c) ALOS-2 descending track coseismic interferogram covering the 28th December 2016 Mochiyama earthquake from Komura et al. [2019]. (d) Sentinel-1 descending track interferogram covering the first month of postseismic relaxation after the 2016 earthquake.

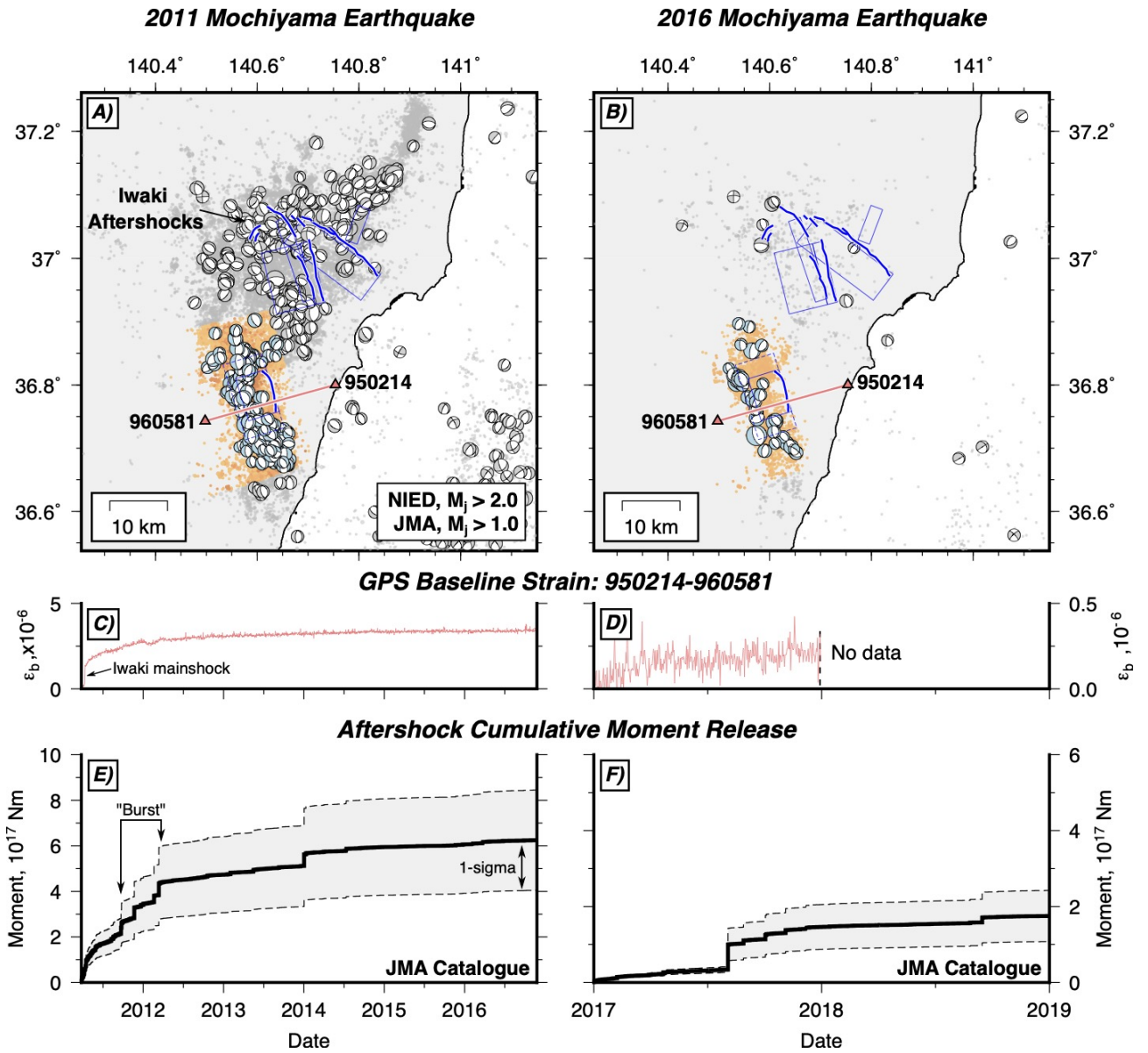


Figure 5: Locations and mechanisms of aftershocks from the JMA unified catalogue and NIED CMT catalogue following the 2011 and 2016 Mochiyama earthquakes. (a) and (b) show the map-view distribution of shallow (<20 km) seismicity relative to the Mochiyama and Iwaki Faults (blue rectangles). Events used in the moment summation in (e) and (f) are shown as gold dots. (c) and (d) show the temporal evolution of baseline strain ε_b between GEONET stations 950214 and 960581 (red triangles in a and b). Note the stark difference in the strain amplitude. (e) and (f) show the temporal evolution of cumulative moment release from aftershocks in the JMA unified catalogue. Uncertainties are shown by the light gray background and result from converting local magnitudes M_j to moment magnitudes M_0 using the scaling of Uchide and Imanishi [2018].

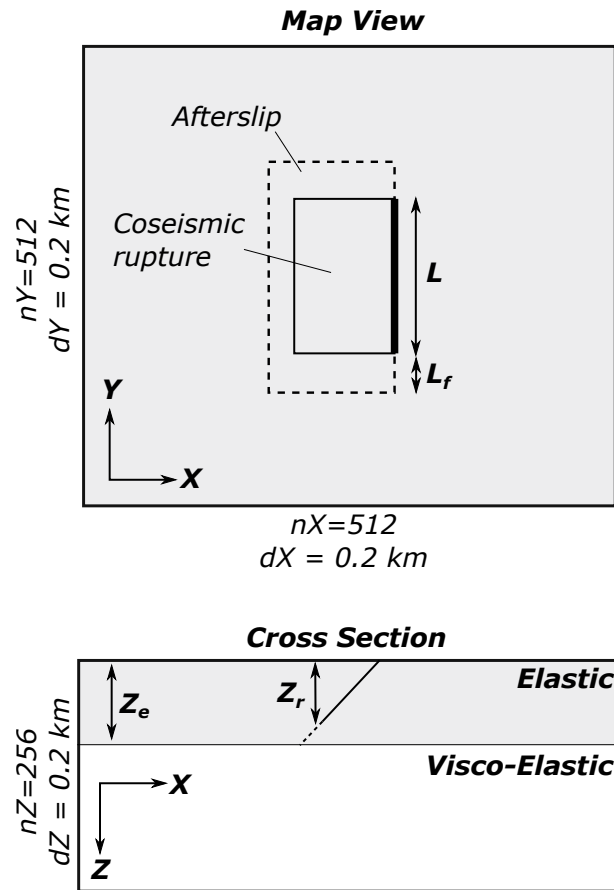


Figure 6: Sketch of the set-up of the generalised numerical calculations in map view (top) and cross-section (bottom). nX , nY and nZ are the number of nodes used in the numerical solutions, and dX , dY and dZ are the spacing between the nodes. The dashed region shows the area of the fault that can slide through postseismic afterslip. The coseismic rupture area is discretised into 8 patches along-strike and 8 patches down-dip.

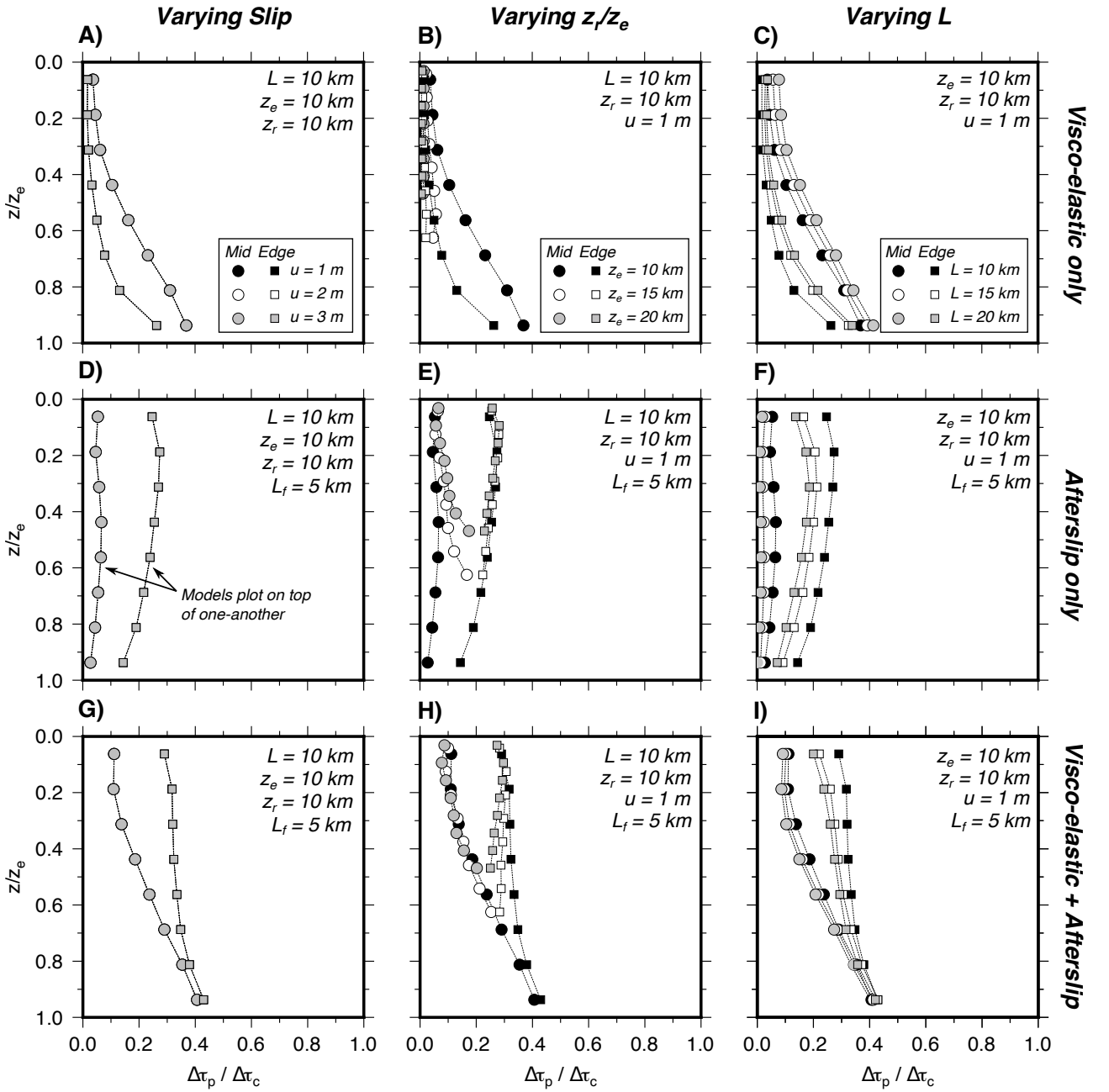


Figure 7: Results of the numerical experiments for the postseismic shear stress recovery $\Delta\tau_p/\Delta\tau_c$ as a function of depth relative to the base of the elastic layer z/z_e when varying the amount of fault slip u (a,d,g), the depth of the fault rupture z_r (b,e,h) and the fault length L (c,f,i). The top row shows models that only include visco-elastic relaxation below $z/z_e > 1$, the middle row shows models that only include frictional afterslip above $z/z_e < 1$, and the bottom row shows models that include both visco-elastic relaxation and afterslip. Circles represent $\Delta\tau_p/\Delta\tau_c$ in the middle of the fault, whilst squares represent $\Delta\tau_p/\Delta\tau_c$ along the lateral edge of the fault. The values of the fixed parameters are shown in the top right of each box.

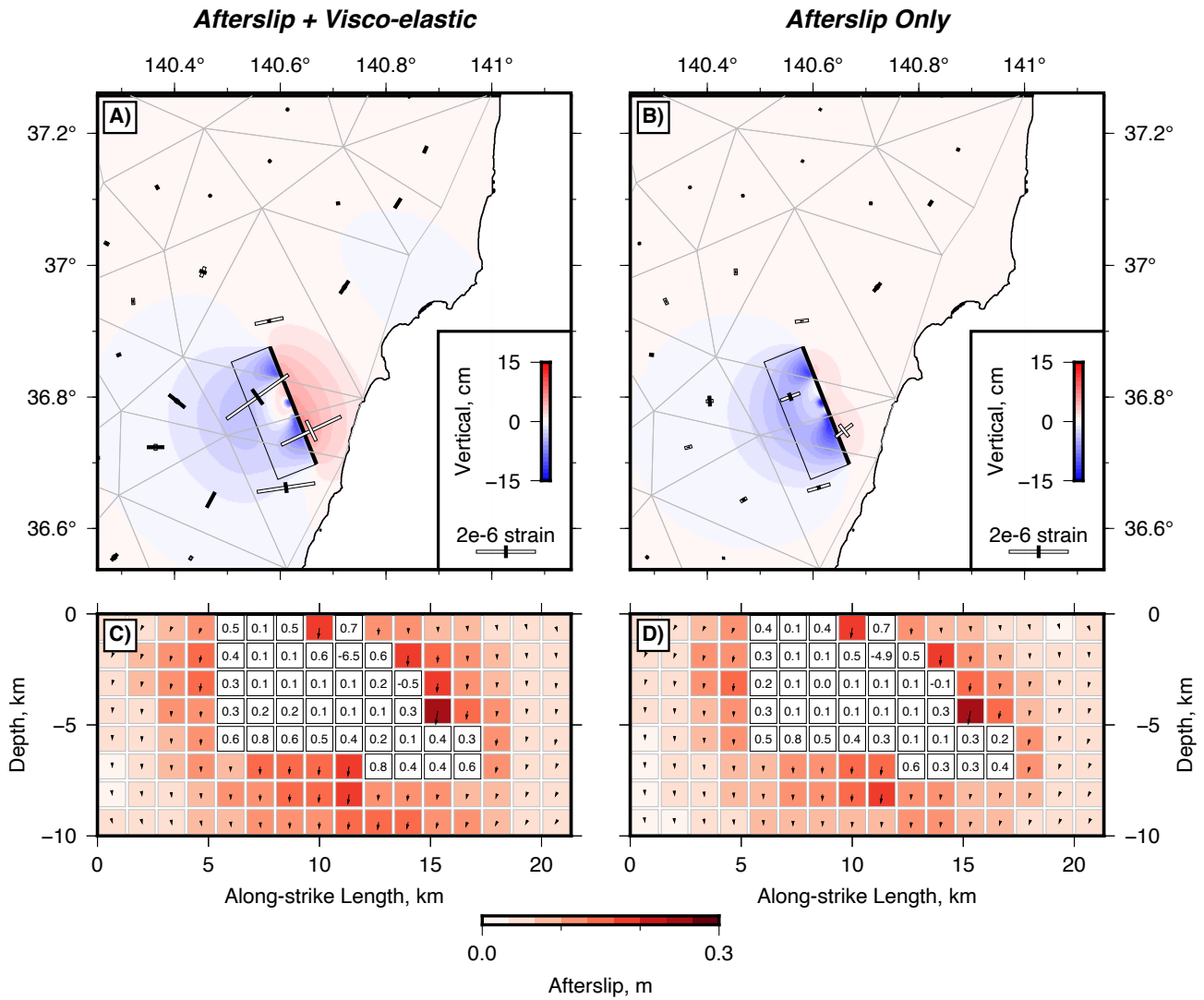


Figure 8: Stress-driven forward models of the postseismic relaxation following the 2011 Mochiyama earthquake. (a) Vertical surface displacements and horizontal strain calculated for a model in which all of the coseismic stress changes are relaxed by afterslip and visco-elastic relaxation. The elastic layer thickness in this calculation is 10 km. (b) The same calculation as in (a), but strain is relaxed by localised shear at depths >10 km and not distributed flow. In (a) and (b) faults are marked by thin black lines, with a thick black line at their up-dip edge. The GPS network is shown by the light grey triangles with GPS stations at their vertices. (c) and (d) show the distribution of afterslip and the shear stress recovery $\Delta\tau_c/\Delta\tau_p$ on the coseismic rupture. Arrows on each afterslip patch show the slip vector and are scaled by the afterslip amplitude.

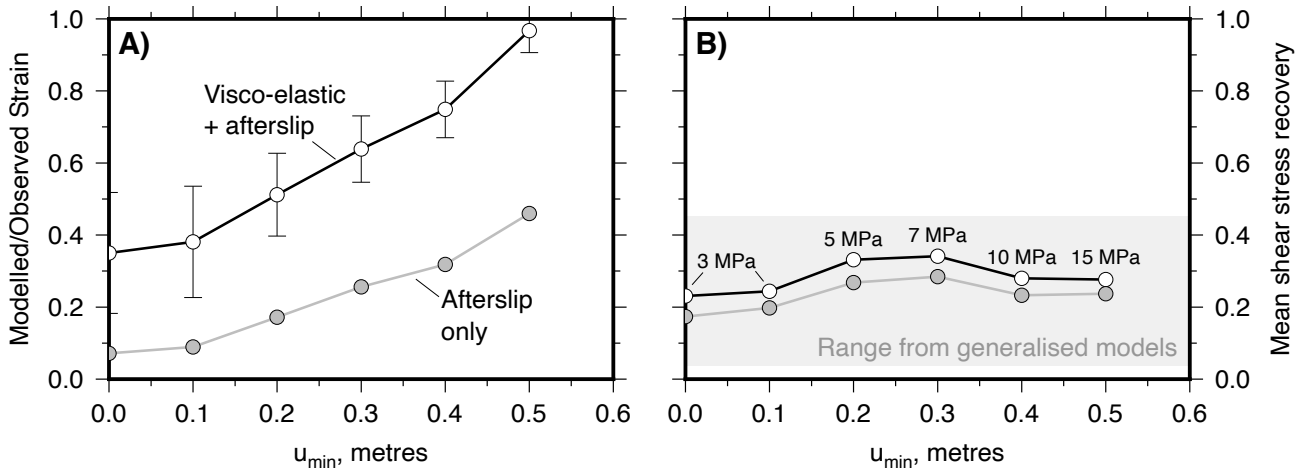


Figure 9: Calculations for the effect of compacting the slip distribution on the observed surface strain and shear stress recovery. (a) Ratio between the modelled and the observed (3.6 microstrain) across-fault extensional strain. Error bars are ± 0.3 microstrain, but are not shown for the afterslip-only models. (b) Mean shear stress recovery over the whole rupture area. The grey background is the range of shear stress recovery inferred from the generalised models. Numbers above each point represent the fault-averaged stress drop for the slip model used to calculate the coseismic stress changes.

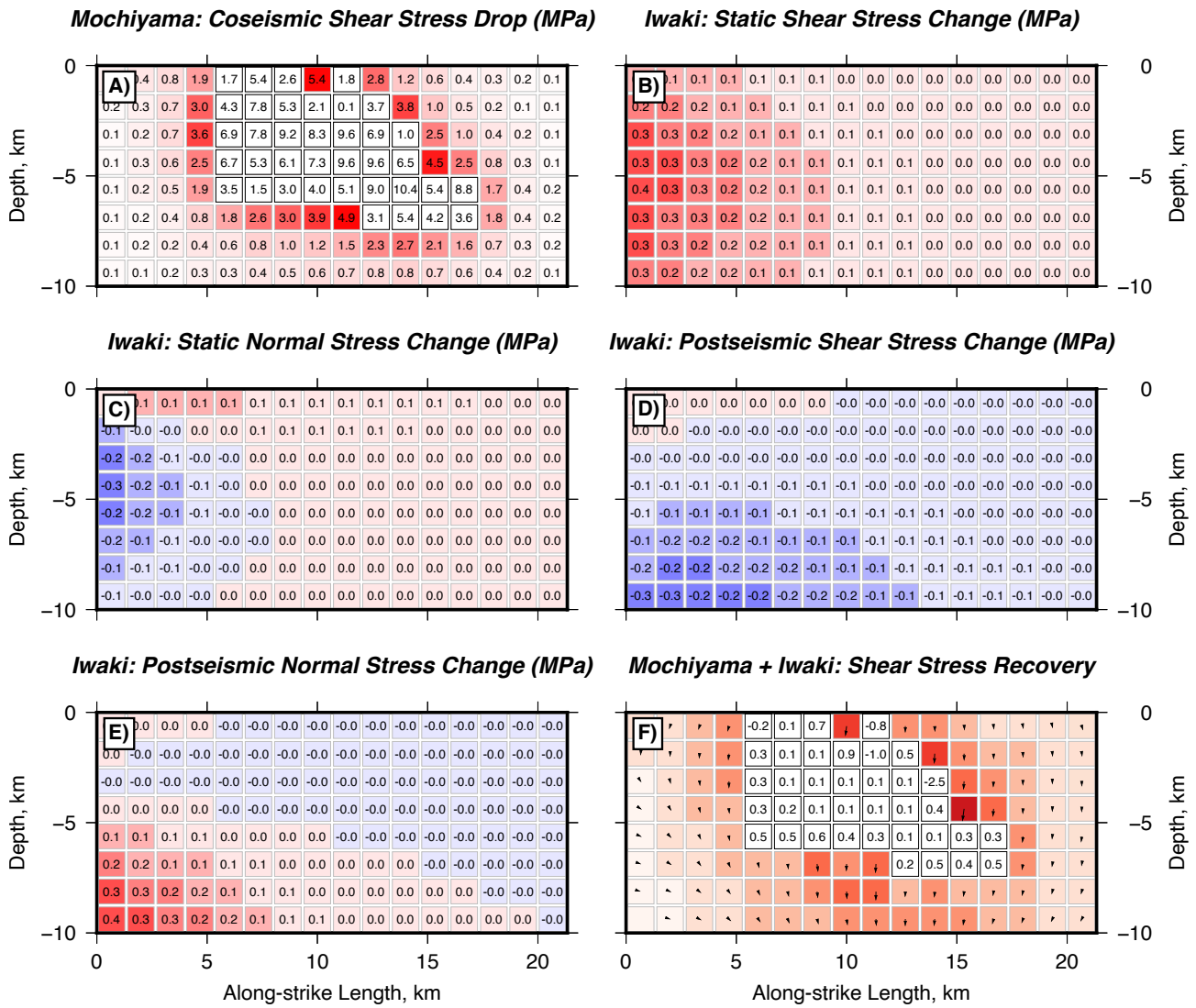


Figure 10: Contribution of the static deformation and postseismic relaxation associated with the Iwaki earthquakes to reloading of the Mochiyama Fault. By convention, shear stress changes are positive if in the direction of slip and normal stress changes are positive for fault clamping. (a) Coseismic shear stress changes from slip on the Mochiyama Fault only. Shear stress (b) and normal stress (c) changes on the Mochiyama Fault due to coseismic slip in the Iwaki earthquakes. Shear stress (d) and normal stress (e) changes due to postseismic relaxation following the Iwaki earthquakes. (f) The pattern of afterslip and shear stress recovery on the Mochiyama Fault due to the relaxation of coseismic stress changes in models that include slip on both the Mochiyama and Iwaki faults. Colour scale for afterslip is the same as that in Figure 8.

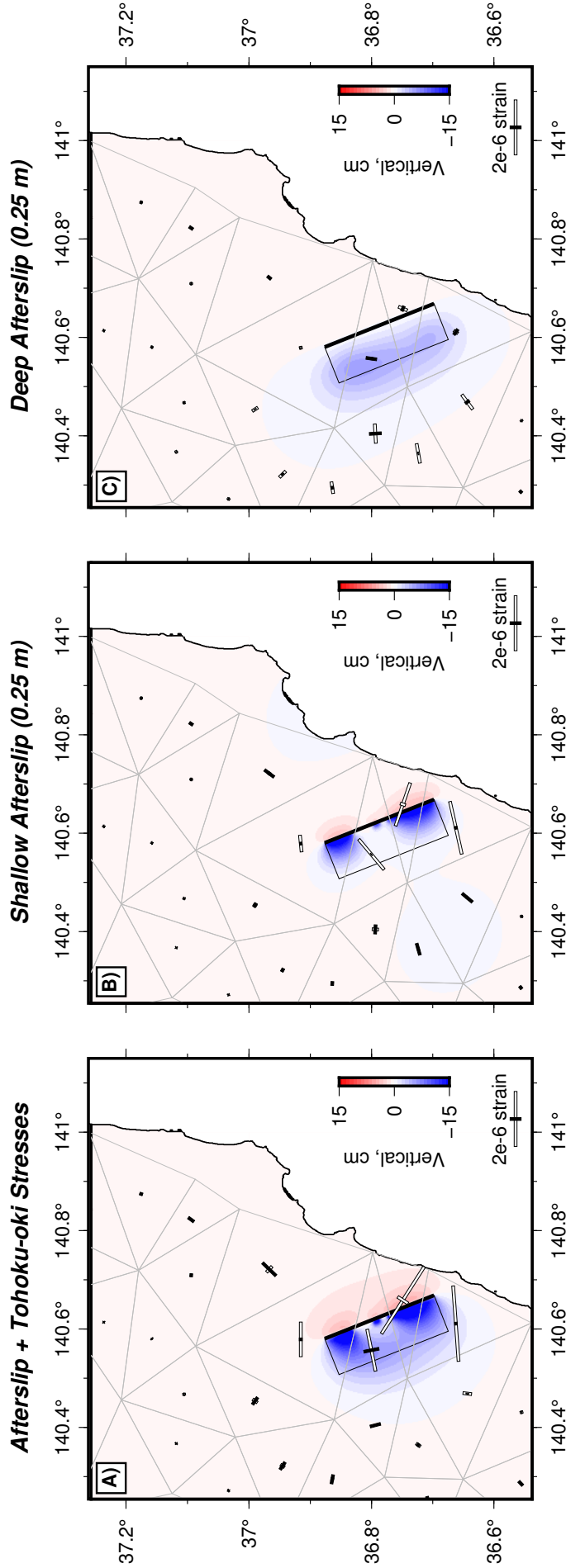


Figure 11: Effect of the Tohoku-oki earthquake on the postseismic deformation around the Mochiyama Fault. (a) Surface strain predicted by a model in which both the coseismic stress changes due to slip in the 2011 Mochiyama earthquake, and the stress changes due to co- and postseismic deformation from the Tohoku-oki earthquake, are relaxed by slip on the Mochiyama Fault. (b) Forward model of the strain predicted for 0.25 m of shallow afterslip on the top 5 km of the Mochiyama Fault. (c) Same as (b) but for 0.25 m of slip in the bottom 5 km of the Mochiyama Fault. Together (b) and (c) highlight that, to account for the observation of contractional strain within GPS triangles in the fault hangingwall, any afterslip must have been relatively shallow.

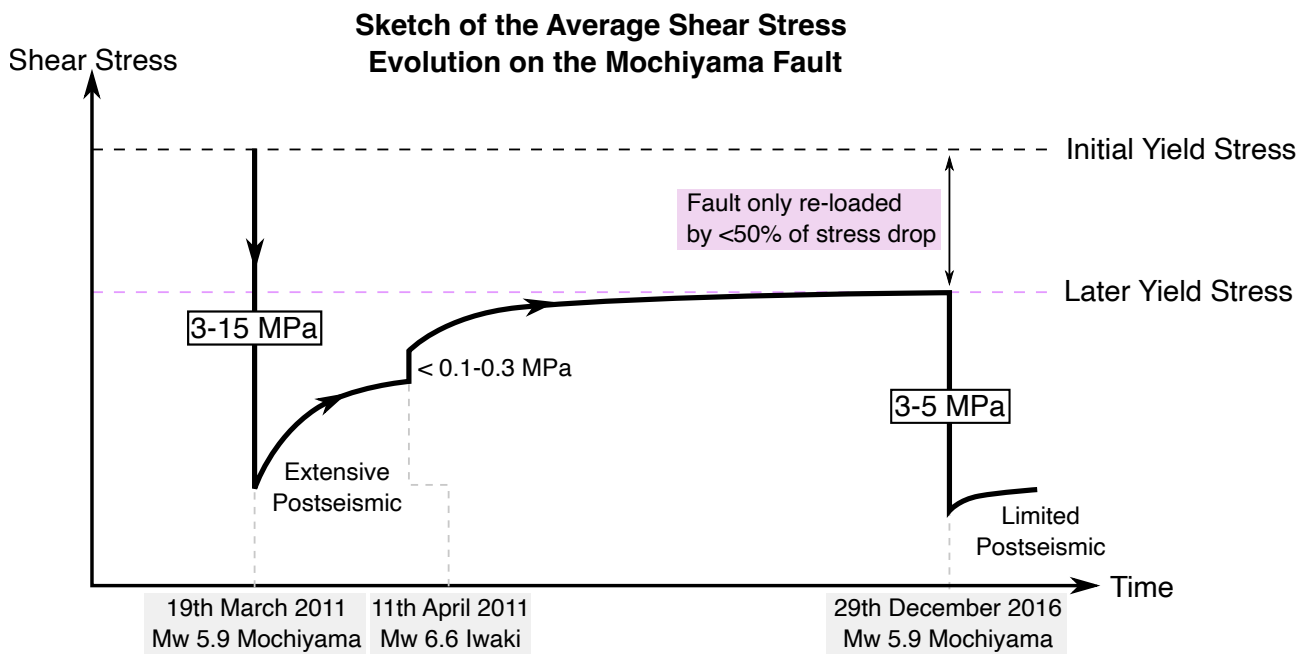


Figure 12: Sketch of the evolution of the fault-averaged shear stress on the Mochiyama Fault between the 2011 and 2016 earthquakes. The stress drop in the 2011 earthquakes and 2016 earthquakes are shown in black boxes, and were calculated from the slip distributions of Fukushima et al. [2018].